

Kristoffer Fjellvikås Solvik

Ship Collision and Earthquake Analysis of Monopile Offshore Wind Turbines

Master's thesis in Marine Technology

Supervisor: Jørgen Amdahl

June 2020

NTNU
Norwegian University of Science and Technology
Faculty of Engineering
Department of Marine Technology



Norwegian University of
Science and Technology

Kristoffer Fjellvikås Solvik

Ship Collision and Earthquake Analysis of Monopile Offshore Wind Turbines

Master's thesis in Marine Technology
Supervisor: Jørgen Amdahl
June 2020

Norwegian University of Science and Technology
Faculty of Engineering
Department of Marine Technology



Norwegian University of
Science and Technology

MASTER THESIS 2020

For

Stud. **Kristoffer Solvik**

Ship collision and earthquake analysis of monopile offshore wind turbines

Analyse av skipsstøt og jordskjelv for offshore vindturbiner understøttet av monopæl

Background;

Wind power is considered to be “green” energy and a large number of wind turbines have been erected on land. However, the wind energy potential is considerably larger in open seas, the environmental impact is smaller, and consequently it is expected that an increasing part of the new wind farms will be installed offshore. Shallow water areas - up to approximately 50 - 70m water depth - will be utilized first as this will allow for bottom supported installations. Development is notably taking place in Sheringham Shoals and Dogger Bank in UK and in the Germany waters of the North Sea and the Baltic Sea.

Wind farms will be serviced by vessels and thus the risk of impacts exists. In addition, many offshore wind farms will be located close to ship traffic lanes and thus the risk of collision with merchant vessel or even large tankers become of concern. For wind turbines supported by monopiles or jackets several failure modes are possible:

- The support structure may be pushed over such that the turbine drops into the sea away from the vessel
- The support structure may collapse at the impact point, so the tower collapse towards the vessel
- The support structure may survive the impact, but local buckling of the tower may take place in the tower, such that it collapses towards or away from the vessel

The objective of this investigation is to examine in more details the response of different bottom supported offshore wind turbines to ship impacts.

Scope of work

The following topics should be addressed:

1. The collision analysis should include the turbine in both parked and operating condition. In the operating condition the inertia effects of the rotating blades should be taken into account using a simple constant pitch model. A beam model of the blades shall be established with correct flexibility. The effect of the wind drag and lift forces shall be modelled with equivalent line loads. The model shall be calibrated against the behaviour of an accurate blade model. The model shall be established for a turbine with at least 10 MW effect, but if data are available a larger turbine shall be selected (12-15 MW).

2. Establish finite element models for the tower and support structure, including soil models. The soil characteristics to be determined in collaboration with supervisors. The support structure should include a jacket, a tripod and a monopile.
3. For large diameter tubes conduct integrated analysis of the damage using LS-DYNA. Finite element models of the impacting ship will be made available.
4. To investigate possible local buckling of the tower at the bottom, this section shall be modelled with shell elements. Local imperfections may need to be established. The local buckling model should be verified against rule formulations.
5. Conduct global analysis of the impact with USFOS, where the local indentation behaviour of the ship and crushing of the ship are modelled with nonlinear springs. Explain the results wrt. to collapse mechanisms and to the extent possible and desired check them with simple methods. Crucial failure mechanisms are: Collapse of support structure, local buckling of tower, accelerations of the nacelle, including fall direction.
6. If this is made possible conduct analysis of glancing blow impacts with representative global motion properties of the ship (waterplane stiffnesses, masses and mass moments of inertia). Compare with simplified uncoupled analysis.
7. Conclusions and recommendations for further work

Literature studies of specific topics relevant to the thesis work may be included.

The work scope may prove to be larger than initially anticipated. Subject to approval from the supervisor, topics may be deleted from the list above or reduced in extent.

In the thesis the candidate shall present his personal contribution to the resolution of problems within the scope of the thesis work.

Theories and conclusions should be based on mathematical derivations and/or logic reasoning identifying the various steps in the deduction.

The candidate should utilize the existing possibilities for obtaining relevant literature.

The thesis should be organized in a rational manner to give a clear exposition of results, assessments, and conclusions. The text should be brief and to the point, with a clear language. Telegraphic language should be avoided.

The thesis shall contain the following elements: A text defining the scope, preface, list of contents, summary, main body of thesis, conclusions with recommendations for further work, list of symbols and acronyms, references and (optional) appendices. All figures, tables and equations shall be numerated.

The supervisor may require that the candidate, in an early stage of the work, presents a written plan for the completion of the work. The plan should include a budget for the use of computer and laboratory resources which will be charged to the department. Overruns shall be reported to the supervisor.

The original contribution of the candidate and material taken from other sources shall be clearly defined. Work from other sources shall be properly referenced using an acknowledged referencing system.

The report shall be submitted in two copies:

- Signed by the candidate
- The text defining the scope included
- In bound volume(s)
- Drawings and/or computer prints which cannot be bound should be organised in a separate folder.

Supervisor:

Prof. Jørgen Amdahl
Postdoc Zhaolong Yu

Deadline: June 10, 2020

Trondheim, January 15, 2020




Jørgen Amdahl

Preface

This master's thesis is the result of the work done during the spring semester of 2020. The thesis marks the end of a five year Master of Science degree in marine technology at the Norwegian University of Science and Technology, Trondheim, Norway. The thesis objectives were formulated in cooperation with Professor Jørgen Amdahl and assigned by the Department of Marine Technology. The idea behind the work is inspired by the ongoing development of the offshore wind industry, combined with the author's interest within the field of ship collisions. The master's thesis is written as part of a specialization within marine structures, and the reader is assumed to have some background within this field.

Trondheim, June 10, 2020

Signature: 
Kristoffer Fjellvikås Solvik

Acknowledgment

I would first and foremost like to thank my supervisor Prof. Jørgen Amdahl for the guidance during this semester. He has given valuable feedback and taken part in good discussions which has enhanced the quality of the work considerably. His continuously interest in the thesis and availability for guidance during the special circumstances of the Covid-19 pandemic, has been motivating for completing the work.

Further, I would like to thank Tore Holmås for valuable help and contributions during the modeling process in USFOS. Establishing the OWT from scratch has been a challenging, but very rewarding task when looking back at the first sketch made in January, to the final outcome presented here. Without his help this process would have been considerably more difficult to carry out.

Next, I would like to thank others at NTNU for the help and feedback. I would like to express my gratitude to PhD Candidate Stian Høegh Sørum for always being available for questions during the semester. His contributions have been especially valuable for understanding the theory behind the wind turbine blades during the modeling process. Also, a big thanks goes to my co-supervisor Postdoc. Zhaolong Yu for the guidance during the analyses in LS-DYNA and when using Vilje.

Finally, a special thanks goes out to all my fellow students and friends from the class of 2020. Even though the final semester unfortunately ended under special circumstances, these past five years have been truly memorable.

Abstract

The offshore wind industry has shown rapid development in recent years. In only two decades, the turbines have grown from being relatively small to becoming huge structures of several hundred meters, generating power for thousands of people. The first part of this report describes the development of the offshore wind turbines in recent years. The increase in size, water depth and distance to shore is used to present the potential challenges it may cause concerning ship impacts from vessels operating in the same area. Ship impact events are of interest as it causes economic loss, property damage, and at worst human injuries.

The major part of this thesis considers finite element modeling and analyses of a monopile supported offshore wind turbine, subjected to ship impacts and an earthquake event. Both parked and operating conditions of the turbine are considered. The main goal is to investigate the different responses of the wind turbine, and to find out if any of the responses are critical concerning the structural integrity. The modeling and analyses are performed using the computer programs USFOS and LS-DYNA. The ship used for the collision is a standard supply vessel of 7500 tons displacement, with a bulbous bow. Two impact velocities of 3m/s and 5m/s are investigated, corresponding to an initial kinetic energy of 37MJ and 103MJ. The ship is modeled to collide head-on in the center of mass of the transition piece of the wind turbine, which is a conservative approach.

The results showed that the offshore wind turbine, in general, has a high resistance against global collapse for all the studied scenarios. The most critical results concerning the failure of the turbine were found to be the forces in the bottom and mid part of the tower and the accelerations of the nacelle. The monopile and transition piece were less affected. The soil utilization was found to be high in the upper layers, but considerably lower in the deeper layers. The operating condition proved to have a positive effect on the soil utilization and a negative effect on the moment force in the bottom part of the tower.

For the most critical scenarios, the tower experienced some local buckling in the bottom and middle part for the collision and earthquake, respectively. However, this did not cause a collapse of the structure. In order to investigate the collapse mechanisms, buckling in these sections were triggered by either reducing the thickness or increasing the loads. All collapse mechanisms were found to be desirable, as they resulted in the wind turbine falling away from the vessel.

Sammendrag

Offshore vindindustri har opplevd en hurtig utvikling de siste årene. På bare to tiår har turbinene vokst fra å være relativt små til å bli enorme strukturer på flere hundre meter som genererer strøm til tusenvis av mennesker. Den innledende delen av denne rapporten beskriver utviklingen av havvind-turbiner som har blitt gjort de siste årene. Økningen i størrelse, vanndybde og avstand til land brukes til å presentere de potensielle utfordringene dette kan medføre. I dette tilfellet er utfordringen skipskollisjoner med fartøyer som opererer i nærliggende områder. Skipskollisjoner med vindturbiner er av interesse fordi det kan forårsake økonomisk tap, materielle skader og i verste fall skader på mennesker.

Hoveddelen av denne avhandlingen tar for seg endelig elementmodellering og analyser av en offshore vindturbin utsatt for skipskollisjoner, i tillegg til en jordskjelvhendelse. Vindturbinen blir analysert i både parkert og operasjonell tilstand. Hovedmålet er å undersøke vindmøllens forskjellige responser, og finne ut om noen av de er kritiske når det gjelder strukturens integritet. Modelleringen og analysene har blitt utført ved hjelp av dataprogrammene USFOS og LS-DYNA. Skipet som brukes til kollisjonene er et standard forsyningsfartøy på 7500 tonn. To kollisjonshastigheter på 3m/s og 5m/s har blitt undersøkt. Dette tilsvarer en initiell kinetisk energi på 37MJ og 103MJ for sammenstøtet. Skipet er modellert for å kolliderer i massesenteret til overgangsstykket mellom monopælen og tårnet til vindturbinen. Dette er en konservativt tilnærmedelse.

Resultatene viser at vindturbinen generelt har høy motstand mot global kollaps for alle de studerte scenariene. De mest kritiske resultatene når det kommer til svikt av turbinen er spenningene som oppstår i nedre og midtre del av tårnet, og akselerasjonen av nacellen på toppen av tårnet. Monopælen og overgangsstykket mellom denne og tårnet ble mindre påvirket av lastene. Utnyttelsen av jordkapasiteten ble funnet til å være høy for de øverste lagene, men betydelig mindre i de dypere lagene. Effekten av den operasjonelle tilstanden viste seg å ha positiv effekt på jordutnyttelsen og en negative effekt på momentkraften i bunnen av tårnet.

For de mest kritiske tilfellene ble det oppservert noe lokal buling i bunnen og den midtre delen av tårnet for henholdsvis den største kollisjonen og jordskjelvet. Selv om dette oppsto, førte det ikke til at strukturen kollapset. For å undersøke kollapsmekanismen

til vindturbinen ble knekkingen utløst enten ved reduksjon av veggtykkelse eller økning av påført last. Alle kollapsmekanismene som oppsto var ønskelig, siden de førte til at vindturbinen falt i motsatt retning av det kolliderende skipet.

Table of Contents

Preface	i
Acknowledgment	iii
Abstract	v
Sammendrag	vii
Table of Contents	xi
List of Tables	xiv
List of Figures	xx
Nomenclature	xxi
1 Introduction	1
1.1 Thesis objectives	2
1.2 Approach for solving thesis objectives	2
1.3 Limitations of study	3
1.4 Main contributions of thesis	3
1.5 Outline	4
2 Background	5
2.1 Key trends and statistics	5
2.2 Bottom supported offshore wind turbines	9

2.2.1	Monopile development	9
2.3	Collision risk	10
2.4	Potential consequences	12
2.4.1	Previous incidents	13
2.5	Literature study	15
3	Design Principles	17
3.1	General	17
3.2	Energy formulations	19
3.2.1	Strength, ductile and shared-energy design	19
3.2.2	External dynamics and internal mechanics	20
3.2.3	Effect of initial imperfections on the buckling strength of cylindrical shells	23
4	Numerical Modeling of Offshore Wind Turbine, Soil and Loads	27
4.1	Reference structure	27
4.2	USFOS model	28
4.2.1	Rotor-nacelle assembly modeling	28
4.2.2	Modeling of blades	30
4.2.3	Tower modeling	32
4.2.4	Modeling of monopile foundation	33
4.2.5	Modeling of soil conditions	35
4.2.6	Modeling of applied loads	38
4.2.7	Ship impact modeling	42
4.2.8	Modeling of earthquake	43
4.2.9	Shell modeling of bottom and midsection of tower	44
4.3	LS-DYNA model	46
4.3.1	Ship modeling for local analysis	46
4.3.2	Modeling of transition piece for local analysis	47
5	Local Analysis of Bow Crushing in LS-DYNA	49
6	Global Analyses of Ship Impacts and Earthquake Loads in USFOS	53
6.1	Impact energy and force-deformation curves	54
6.2	Analysis of ship collision with parked OWT	56
6.2.1	Tower top acceleration	57
6.2.2	Moment force in bottom of tower	58
6.2.3	Soil utilization	60

6.3	Analysis of ship collision with OWT in operating condition	62
6.3.1	Tower top acceleration	62
6.3.2	Clearance between blade tip and tower	63
6.3.3	Moment force in bottom of tower	65
6.3.4	Soil utilization	66
6.4	Comparison of impact response between parked and operating condition .	67
6.4.1	Tower top acceleration	67
6.4.2	Moment force in bottom of tower	68
6.4.3	Soil utilization	70
6.5	Analysis of earthquake loads on OWT	70
6.5.1	Tower top acceleration	71
6.5.2	Clearance between blade tip and tower	72
6.5.3	Moment force in bottom section of tower	73
6.5.4	Comparison between the structural response and the mode shapes and natural frequencies of the OWT	74
7	Local Buckling Analyses of the OWT Tower	79
7.1	Simple calculations of buckling capacity	79
7.1.1	Bottom part of tower	80
7.1.2	Mid part of tower	81
7.2	Overview of results from the global analyses	82
7.2.1	Results from collision analyses	82
7.2.2	Results from earthquake analyses	83
7.3	Comparison between imperfection application methods	84
7.4	Buckling response during ship collision	85
7.5	Buckling response during earthquake	88
8	Conclusions and Recommendations for Further Work	91
8.1	Conclusions	91
8.2	Recommendations for further work	93
	Bibliography	95
	Appendix	99

List of Tables

4.1	Main characteristics of RNA. (Bak et al., 2013)	29
4.2	Comparison of natural frequencies of isolated blades between model and the reference wind turbine of Bak et al. (2013).	31
4.3	Main characteristic dimensions of the OWT tower.	32
4.4	Comparison of natural periods between monopile-mounted OWT model and similar model of Horn (2018).	38
6.1	A selection of natural frequencies and corresponding vibration modes obtained from the eigenvalue analysis of the complete OWT model performed in USFOS.	76
7.1	Main dimensions of bottom part of tower used in buckling capacity calculations.	80
7.2	Main dimensions of mid part of tower used in buckling capacity calculations.	81
7.3	Maximal obtained bending stress in bottom section of tower when subjected to ship collision events. Stresses exceeding the buckling stress are marked with bold text.	82
7.4	Maximal obtained bending stress in mid section of tower when subjected to ship collision events. Stresses exceeding the buckling stress are marked with bold text.	82
7.5	Maximal obtained bending stress in bottom section of tower when subjected to earthquake events. Stresses exceeding the buckling stress are marked with bold text.	83

7.6 Maximal obtained bending stress in mid section of tower when subjected to earthquake events. Stresses exceeding the buckling stress are marked with bold text.	83
--	----

List of Figures

2.1	Annual offshore wind installations by country and cumulative capacity (GW) in Europe. (WindEurope, 2020)	6
2.2	Timeline of average water depth of online offshore wind farms in Europe the past 20 years. (WindEurope, 2020)	6
2.3	Timeline of average distance to shore of online offshore wind farms in Europe the past 20 years. (WindEurope, 2020)	7
2.4	OWT foundations installed in Europe in 2019 by manufacturing company. (WindEurope, 2020)	7
2.5	Number of OWT foundations by substructure type in European wind farms as of early 2020. (WindEurope, 2020)	8
2.6	Definition of bottom fixed offshore wind turbine components. (DNV GL, 2016)	9
2.7	XL Monopile specifications for OWTs used at the Merkur Offshore wind farm. (Merkur Offshore)	10
2.8	Overview of European offshore wind farms as of early 2020. (WindEurope)	11
2.9	Overview of marine traffic density in areas of European offshore wind farms. (MarineTraffic)	11
2.10	OSV damage after collision with OWT transition piece under construction. (Federal Bureau of Maritime Casualty Investigation, 2019)	14
2.11	Big Orange bow damage after collision with water injection platform on the Ekofisk field. (Petroleumstilsynet, 2009)	14

3.1	Energy dissipation for strength, ductile and shared-energy design (DNV GL, 2017)	20
3.2	Strain energy dissipation in ship and platform during a collision event. (DNV GL, 2017)	21
3.3	Recommended force-deformation curves for beam, bow and stern impacts for standard supply vessels of 6500-10000 tons. (DNV GL, 2017)	22
3.4	Force-deformation relationship for bow impacts from supply vessels with displacement 5-10.000 tonnes - standard bulbous bow with no ice-reinforcement and ICE-1C class. (DNV GL, 2017)	22
3.5	Theoretical load-end shortening curve showing equilibrium paths for perfect and imperfect shells subjected to axial compression. B marks the intersection between the stable and unstable state and is called the bifurcation point.(Amdahl, 2010)	23
3.6	Influence of axisymmetric imperfections on the buckling load of an axially loaded cylinder.(Amdahl, 2010)	24
3.7	Definition of factors used for calculating maximum imperfections in equation 3.3.(DNV GL, 2015)	25
4.1	Key parameters of the DTU 10MW Reference Wind Turbine. (Bak et al., 2013)	28
4.2	Representation of the model simplifications of the RNA and tower-blade connection in USFOS.	29
4.3	Beam model of OWT blades in USFOS representing structural and visual properties.	31
4.4	Complete structural model of OWT including the tower, RNA and blades.	33
4.5	Pipe with 8 integration points along the circumferential. (USFOS, 2019)	34
4.6	Generated monopile model including representation of the soil layers.	35
4.7	Random field model of soil including sources of uncertainty. (Smilden et al., 2020)(adapted from Phoon and Kulhawy (1999))	36
4.8	Three-layered field model properties applied to soil model in USFOS. (Smilden et al., 2020)	36
4.9	Soil utilization of OWT while in operating condition with applied wind loads.	37
4.10	Vibrational modes of monopile-mounted OWT model. Scaled up for visualisation purposes. Soil is included.	38
4.11	Gradual increase of the rotational speed of the OWT blades in operating condition.	39

4.12	Blade forces on a foil cross section of a wind turbine blade. (Manwell et al., 2010)	40
4.13	Simplified wind load model representing the distribution and magnitude of nodal loads applied along the OWT blades.	41
4.14	Spring system representing the force-deformation curves applied in the collision analysis in USFOS, with column representing ship mass and added mass.	43
4.15	Soil displacement history applied in earthquake analysis on OWT.	44
4.16	Shell representation of the bottom part of the OWT tower with mesh, used in the buckling analysis when subjected to ship impact.	45
4.17	Visual representation of the two different models used for introducing initial imperfections in the tower in the structural model. Up-scaled for visual purposes.	46
4.18	Finite element model of supply vessel bow used in bow crushing analysis in LS-DYNA.	46
4.19	Finite element model of supply vessel bow and rigid cylinder for obtaining force-deformation curves for forecastle.	48
4.20	Finite element model of supply vessel bow and rigid cylinder for obtaining force-deformation curves for bulb.	48
5.1	Deformation of the forecastle before and after the crushing analysis.	50
5.2	Deformation of the bulb before and after the crushing analysis.	50
5.3	Force-deformation curves for forecastle and bulb obtained from bow crushing analysis in LS-DYNA. Linear approximation to be applied in global USFOS analysis is included.	51
5.4	Main elements contributing to stiffening of the ship bow section.	52
6.1	Kinetic energy obtained in USFOS for the two impact speeds resulting in collision energies of 37MJ and 103MJ on the OWT.	54
6.2	Comparison between input force-deformation curves for forecastle and curves obtained from USFOS analyses.	55
6.3	Comparison between input force-deformation curves for bulb and curves obtained from USFOS analyses.	55
6.4	Acceleration of the tower top for the two ship impact scenarios with the parked OWT.	57
6.5	Moment force in the bottom part of the tower for the two ship impact scenarios with the parked OWT.	58

6.6	Snapshots showing the displacement of the OWT tower at the points obtaining the largest moment force values at the bottom part of the tower. Up-scaled deformations for visual purposes.	59
6.7	Snapshots showing the plastic utilization factors of the OWT tower at the points obtaining the largest moment force values at the bottom part of the tower. Up-scaled deformations for visual purposes. The fringe ranges from 0 (dark blue) to 1 (red).	60
6.8	Soil utilization comparison between the two ship impact scenarios for the parked OWT.	60
6.9	Highest soil utilization for largest ship collision event on the parked OWT.	61
6.10	Acceleration of the tower top for the two ship impact scenarios with the OWT in operating condition.	62
6.11	Relative horizontal distance between blade tip and tower for OWT in operation, before and after the impacts. Impacts are applied after 60s. Extra tower clearance is added to account for the neglected cone and tilt angle in the model.	63
6.12	Close-up of relative horizontal distance between tower and blade tip for OWT in operation, subjected to the ship impacts. The blue dotted line defines the contact point between the blade tip and tower.	64
6.13	Moment force in the bottom part of the tower for the two ship impact scenarios with the OWT in operating condition.	65
6.14	Soil utilization comparison between the two ship impact scenarios for the operating OWT.	66
6.15	Maximum soil utilization during largest ship collision event on the OWT in operation.	66
6.16	Comparison between parked and operating OWT tower top acceleration when subjected to 3m/s ship collision event.	67
6.17	Comparison between parked and operating OWT tower top acceleration when subjected to 5m/s ship collision event.	68
6.18	Comparison between parked and operating OWT tower top acceleration when subjected to 3m/s ship collision event.	68
6.19	Comparison of moment force in bottom part of tower between parked and operating OWT, subjected to 5m/s ship collision event.	69
6.20	Effect of operating condition on the soil utilization for the two collision scenarios.	70

6.21	Time history of tower top acceleration in global y-direction during earthquake on OWT in parked condition.	71
6.22	Relative horizontal distance between tower and blade tip for OWT in operation, subjected to earthquake. The blue dotted line defines the contact point between the blade tip and tower.	72
6.23	Time history of moment force in bottom part of tower during earthquake on OWT in parked condition.	73
6.24	Time domain of the soil displacement history of the earthquake.	74
6.25	Frequency domain of the soil displacement history of the earthquake. Displacement amplitudes are normalized on the y-axis.	74
6.26	Frequency domain of the relative displacement history between the pile and the tower top of the parked OWT subjected to the earthquake. Displacement amplitudes are normalized on the y-axis.	75
6.27	Frequency domain of the relative displacement history between the pile and the blade tip of the parked OWT subjected to the earthquake. Displacement amplitudes are normalized on the y-axis.	75
6.28	Snapshots showing the actual response of the OWT during the earthquake. Up-scaled for visual purposes.	77
6.29	Snapshots showing the modal shapes of the OWT. To be compared with the actual response in figure 6.28. Up-scaled for visual purposes.	78
7.1	Comparison of the strain distribution between the two imperfection application methods used in the buckling analyses in USFOS. Fringe ranges from -0.013 (dark blue) to 0.002 (red).	84
7.2	Plastic utilization of bottom and mid section at most critical point during the largest ship impact scenario with the parked OWT. Red color represents full plastic utilization.	85
7.3	Close up of equivalent strain of bottom and mid section at most critical point during the largest ship impact scenario for the parked OWT. Fringe ranges are equal for both cases for comparative purposes. Fringe ranges from -0.005 (dark blue) to 0.003 (red).	86
7.4	Buckling collapse of the OWT as a result of a 10% reduction of the wall thickness of the tower. The deformations are scaled up for visual purposes.	87
7.5	Snapshots showing the evolution of the buckling of the bottom part of the OWT tower. The colors represents the plastic utilization factor, and ranges from 0 (dark blue) to 1 (red).	87

7.6	Close-up of plastic utilization and equivalent strain of mid section at most critical point during the earthquake on the parked OWT. Fringe ranges from 0 (dark blue) to 1 (red) for the plastic utilization factor and from -0.007 to 0.003m for the equivalent strain.	88
7.7	Buckling collapse of the OWT as a result of the earthquake scaled up by a factor of 2. The deformations are scaled up for visual purposes.	89
7.8	Snapshots showing the evolution of the buckling of the mid part of the OWT tower. The colors represents the plastic utilization factor, and ranges from 0 (dark blue) to 1 (red).	89

Nomenclature

Abbreviations

ALS	Accidental limit state
API	American Petroleum Institute
BEM	Blade element momentum
CFD	Computational fluid dynamics
COV	Coefficient of variation
CTV	Crew transfer vessel
DNV GL	Det Norske Veritas Germanischer Lloyd
DTU	Technical University of Denmark
EU	European Union
FLS	Fatigue limit state
FPSO	Floating production, storage and offloading
GW	Gigawatt
MSL	Mean sea level
MW	Megawatt
NORSOK	Norsk Søkkel Konkurransesjjon

NOMENCLATURE

NTNU	Norwegian University of Science and Technology
OSV	Offshore supply vessel
OWT	Offshore wind turbine
RNA	Rotor-nacelle assembly
RWT	Reference wind turbine
SLS	Serviceability limit state
UK	United Kingdom
ULS	Ultimate limit state
US	United States
XL	Extra large

Greek letters

$\bar{\lambda}$	Reduced slenderness factor
δ	Imperfection
ϕ	Plasticity reduction factor
ρ_k	Knock-down factor
σ_E	Elastic buckling stress
σ_y	Yield stress
σ_{cr}	Critical buckling stress

Roman letters

a_i	Axial induction factor
dw_i	Deformation of installation
dw_s	Deformation of ship
E_s	Total strain energy dissipation
$E_{s,i}$	Strain energy dissipation in installation

$E_{s,s}$	Strain energy dissipation in ship
f_n	Natural frequency
R_i	Resistance of installation
R_s	Resistance of ship
T_n	Elastic modulus
T_n	Natural period
U_1	Wind speed far upstream of OWT
U_2	Wind speed at rotor blades
a	Ship added mass
D	Diameter
m	Ship mass
r	Radius
t	Thickness
v	Velocity

Chapter 1

Introduction

As the world population is growing and becoming more prosperous, the demand for energy to power homes, industries, and the economy is increasing. At the same time, sustainability and the desire for a transition from fossil fuels to more environmentally friendly energy sources have increased in the last couple of years. Producing a sufficient energy supply from sustainable sources is a significant challenge for the energy industry today, and offshore wind energy has shown potential and rapid development in recent years.

A large number of wind turbines are installed on land, but the energy potential is significantly larger in open seas. It is also considered to have a smaller environmental impact. As a result of this, combined with significant cost reductions, an increasing amount of wind farms have been installed offshore in recent years. According to WindEurope (2020), trends show that the next generation of offshore wind turbines (OWTs) increase in size, as well as utilizing sites with increasing water depth and distance to shore. The rapid development in size and the increasing amount of OWTs presents new challenges that need to be addressed.

The majority of the installed OWTs are located in the proximity of ship lanes. Besides, the wind farms are serviced by vessels. Thus, the risk of impacts exist. Even though OWTs are unmanned, unlike most offshore oil platforms, there is still a risk of personnel injuries, property damage, economic loss, or pollution if the structure fails. It is thus necessary to assess the response and potential consequences an impact with these next-generation large-volume OWTs can cause.

1.1 Thesis objectives

The original objectives of the thesis were prepared in cooperation with the main supervisor at the start of the semester. These are presented at the beginning of this text. The scope of work has been discussed throughout the work period, and new opportunities have become available along the way. In combination with time limitations, there have been some modifications to the original scope of work after approval from the supervisor. The modifications mainly include three changes:

1. The analyses will solely focus on the monopile foundation due to time limitations on modeling of the jacket and tripod foundations. This reduces part 2 in the original scope of work.
2. After guidance from the supervisor, it was found interesting to investigate the response of the monopile-mounted wind turbine to earthquake loads. This is added to the scope of work. Also, part 4 of the original scope of work is extended to include buckling analyses of the mid-part of the tower when subjected to the earthquake.
3. Due to the above-mentioned modifications and additions, it was decided to remove part 6 from the original scope of work.

1.2 Approach for solving thesis objectives

The approach that has been used to meet the stated thesis objectives is mainly divided into three parts:

1. An extensive literature study of relevant topics related to the objectives has been performed to create a solid foundation for further work. This includes getting familiar with relevant rules and standards, the theory regarding ship collision mechanics, manuals for analysis software to be used, and basic theory about offshore wind.
2. Modeling of the structure to be used in the analyses has been the major part of this thesis work. Learning new software and the iterative process of creating a realistic and representative model from scratch has been time-consuming and important for obtaining reliable results.
3. Local and global analyses have been performed by the use of the software programs USFOS and LS-DYNA, to obtain the results that are presented.

1.3 Limitations of study

The finite element analyses that have been carried out have high demands on computational and storage capacity and have put some limits on what is possible to achieve on a regular computer. As a result of this, some trade-off has been done to lower computational time for some analyses, but not to the extent that results are greatly affected. This mainly applies to the size of finite elements and time steps in the most extensive analysis problems that includes shell elements. There is also no escaping the fact that the current Covid-19 pandemic has created unusual circumstances for many and, to some extent, limited some resources that normally are available.

1.4 Main contributions of thesis

The main contributions of this master thesis consists of the following:

- A representative finite element model of a 10MW offshore wind turbine, mounted on a monopile foundation, has been created using the computer software USFOS. This includes modeling of the blades, tower, transition piece, monopile, and soil characteristics. The modeling of the tower and blades has been done in collaboration with another student using the same OWT for a floating foundation.
- A simplified method for the representation of wind drag- and lift forces on the blades has been modeled by the use of nodal loads on the blade sections.
- The structural model is created to be used in both a parked and operational condition.
- A local analysis have been conducted in LS-DYNA to check the relative strength and deformation of a supply vessel of 7500 tons displacement with a bulbous bow, when subjected to a collision with the modeled offshore wind turbine.
- A global analysis of the ship impact is conducted in USFOS for impact speeds of 3m/s and 5m/s, resulting in collision energies of respectively 37MJ and 103MJ. The crushing of the ship is included in the model by nonlinear springs, using force-deformation curves obtained from the local analysis in LS-DYNA.
- A global analysis of an earthquake scenario has been conducted for the offshore wind turbine model, using given load histories from a previous event.
- An examination of the global response of the offshore wind turbine to the accidental events of the ship collision and earthquake scenarios have been conducted.

- The local buckling behavior of the bottom- and mid-section of the tower has been investigated for the collision and earthquake events.

1.5 Outline

The remaining part of this report is organized in a total of 7 chapters, consisting of the following:

- Chapter 2 presents the background and motivation for this thesis. The chapter contains a description of the development of the offshore wind industry and potential challenges concerning collision events with offshore wind turbines. A brief literature study of relevant previous work is also presented.
- Chapter 3 contains the governing design philosophies from relevant codes, and the theory behind ship impact mechanics.
- Chapter 4 describes the entire modeling process of the numerical offshore wind turbine model with the associated loads and soil conditions, used in the analyses.
- Chapter 5 describes the local analysis and results of the bow crushing of a supply vessel when impacting the offshore wind turbine.
- Chapter 6 contains the global analyses and results of the offshore wind turbine subjected to different ship collision events, in addition to an earthquake scenario.
- Chapter 7 presents local buckling analyses of the sections found to be critical from the global analyses in chapter 6.
- Chapter 8 includes the conclusion of this master's thesis and gives recommendations for further work on the subject.

Background

This chapter presents the different aspects that have been the motivation behind the stated research objectives and specify why it is of interest to investigate. Key trends and statistics are presented to show the rapid development of the offshore wind industry in recent years. Further on, a brief description of bottom supported offshore wind turbines is given. Emphasis is made on the structural dimensions of the next generation monopile-mounted OWTs with a rated capacity of 10MW and beyond. Relevant collision scenarios and potential consequences are described, before a literature study of relevant previous work is presented.

2.1 Key trends and statistics

According to WindEurope (2020), Europe added 3.6GW of new offshore wind capacity in 2019. In total, Europe reached a capacity of 22.1GW at the end of 2019, which is spread across 110 offshore wind farms in 12 countries. The North Sea registered the largest amount of grid connections in Europe in 2019, with over 99% of all installations. The UK and Germany account for the majority of offshore wind capacity in Europe, with respectively 45% and 34% of all installations. An illustration of this can be seen in Figure 2.1.

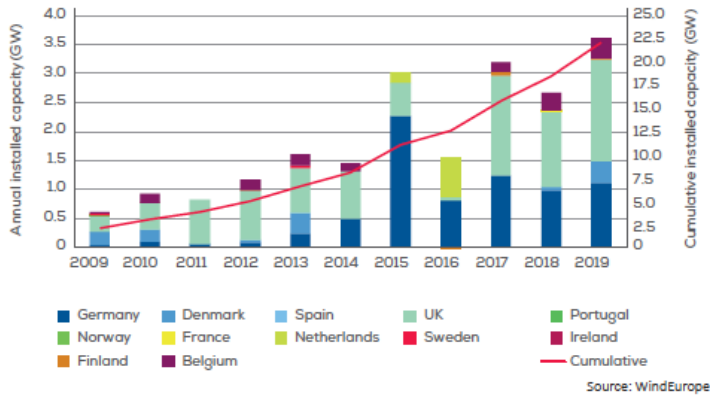


Figure 2.1: Annual offshore wind installations by country and cumulative capacity (GW) in Europe. (WindEurope, 2020)

Areas with shallow water are by far the most utilized for installation of offshore wind farms, as the small depths allow for bottom supported structures. The average water depth of offshore wind farms under construction in 2019 was 33m, with average distance to shore being 59km. The development of average water depth and distance to shore for offshore wind farms for the past two decades can be seen in Figure 2.2 and 2.3.

Even though the average water depth and distance to shore continue to increase, most wind turbines are still bottom-fixed. Monopiles and jacket substructures are the most popular and represent 70% and 29% off all installed foundations in 2019, respectively. In total, monopiles remain the most used foundation with 81%, followed by jackets having 9%. An overview of the installed substructures can be seen in Figures 2.4 and 2.5.

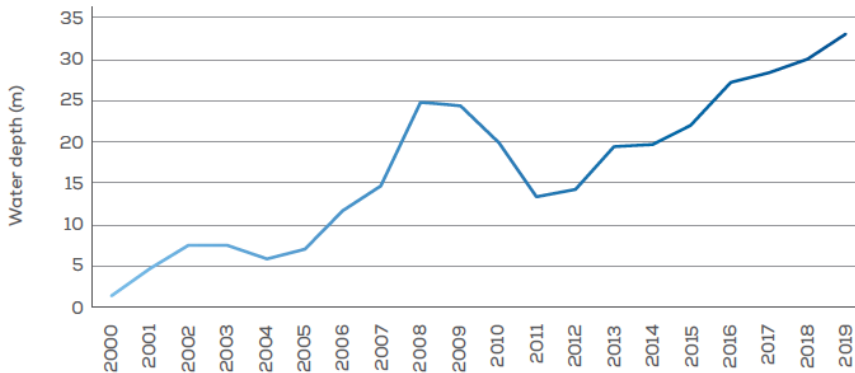


Figure 2.2: Timeline of average water depth of online offshore wind farms in Europe the past 20 years. (WindEurope, 2020)

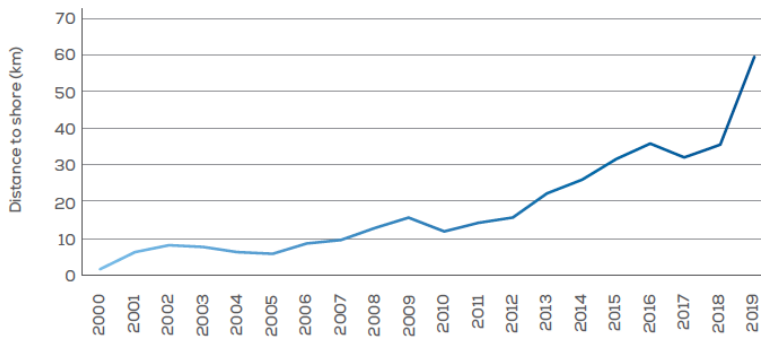


Figure 2.3: Timeline of average distance to shore of online offshore wind farms in Europe the past 20 years. (WindEurope, 2020)

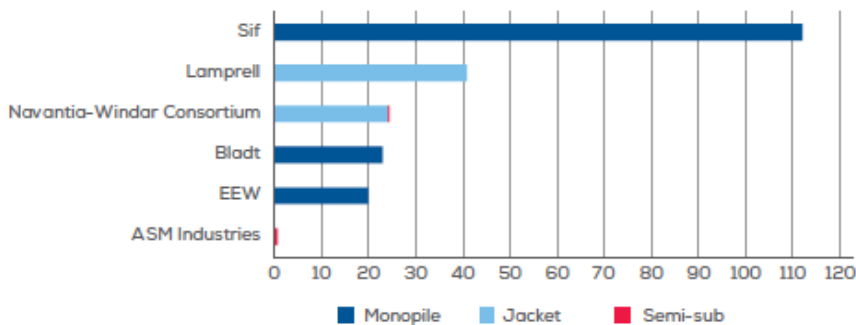


Figure 2.4: OWT foundations installed in Europe in 2019 by manufacturing company. (WindEurope, 2020)

The primary cost-reducing measure of the offshore wind industry has been to increase the swept area and building larger turbines. The size increase leads to higher energy output from each installation, which in turn reduces the number of units that need to be installed. Since 2010 the average rated capacity of the turbines has increased from around 3MW to 7.8MW in 2019. Since 2014 the average rated capacity of newly installed wind turbines has grown at an annual rate of 16%, and trends show that sizes will continue to increase. The largest installed offshore wind turbine in the world today is 9.5MW. The largest commercially available turbine is the 12MW Haliade-X prototype, which was recently installed at a test site in the harbor of Rotterdam by GE Renewable Energy. During the final period of this work, Siemens Gamesa (2020) announced a 14MW OWT with up to 15MW capacity using power boost functions. The turbine is supposed to be ready for serial production in 2024. This also shows the rapid development that is taking place on the subject.

The statistics presented here mainly apply to Europe and are retrieved from WindEurope (2020), but the trends of new OWTs can also be seen in projects outside of Europe. It is worth mentioning that large projects are under development in both Asia and the US. The Empire Wind project southeast of Long Island in the US is mentioned as an example. According to Equinor (2019), it is expected to consist of 10-15MW turbines at water depths of 20-40m. This project is one of several future projects that have the characteristics that this thesis addresses.

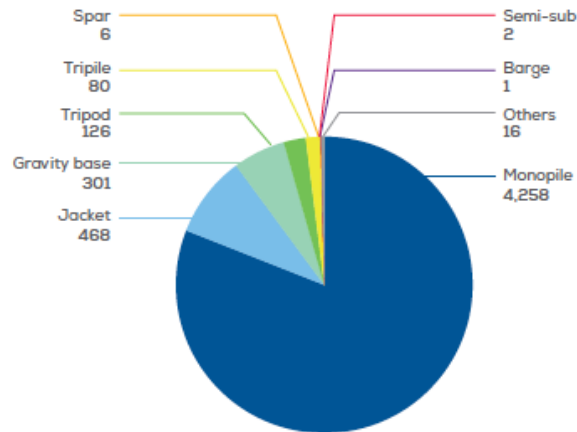


Figure 2.5: Number of OWT foundations by substructure type in European wind farms as of early 2020. (WindEurope, 2020)

2.2 Bottom supported offshore wind turbines

As mentioned earlier, varieties of bottom supported OWTs are by far the most widely used today. Common for all types is that they mainly consist of two parts: the support structure and the rotor-nacelle assembly (RNA), as shown in figure 2.6. The RNA houses all the generating components and the rotor blades. The support structure consists of three parts: the tower, substructure, and foundation. The foundation includes the locally fixed integration into the seabed.

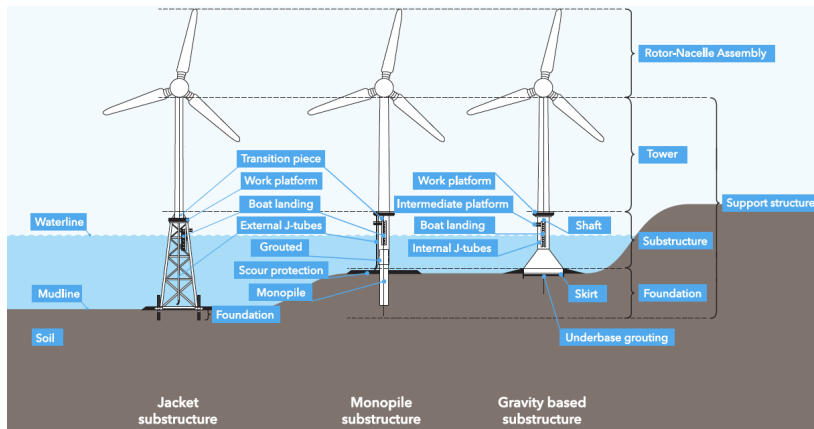


Figure 2.6: Definition of bottom fixed offshore wind turbine components. (DNV GL, 2016)

2.2.1 Monopile development

The monopile substructure is a simple design by which the tower is supported by one large pile, anchored into the seabed. Due to the simple geometry, it allows for rather simple calculations, easier manufacturing, and the possibility to be stacked tightly on the service vessels for transport. The installation is done by hammering the monopile (steel tube) into the seabed and fitting a transition piece on top to fit the rest of the tower and turbine. The transition piece is essential as it transfers loads and moments from the tower to the foundation. Mainly bolting and grouting is used to fix the transition piece.

The dimensions of the monopile varies considerably based on application and water depth, and has increased considerably in recent years. Looking back at the end of 2012, the monopiles supporting OWTs ranged from 2.5-6.0m in diameter and had a limit of 25-30m depth according to Windpower International (2013). At larger depths, the jacket foundation has originally been dominant, but in later years, the emergence of so-called XL monopiles have challenged the jackets at deeper waters.

The XL monopiles have significantly larger dimensions than the monopiles that have commonly been used. Sif Group (2020), one of the leading suppliers of offshore foundations for wind turbines, states that they have the production capacity to produce monopiles up to 11m in diameter with a maximum length and weight of respectively 120 meters and 2000 tons. An example of the use of XL monopiles at deeper waters is the Gemini wind farm off the coast of the Netherlands. Here, monopiles are used at water depths of up to 37 meters (Ramboll Group). Another example is the Merkur offshore wind farm in Germany, which was completed in 2018. The dimensions of the monopiles used in this farm can be seen in figure 2.7.



Specifications

Length	58.5 m – 72.6 m
Embedment length	25 m – 35.4 m
Bottom diameter	7.6 m – 7.8 m
Top diameter	6.0 m
Weight	703 t – 970 t

Figure 2.7: XL Monopile specifications for OWTs used at the Merkur Offshore wind farm. (Merkur Offshore)

2.3 Collision risk

In figure 2.8, an overview of all European offshore wind farms is shown. Below, in figure 2.9, the marine traffic density in the corresponding areas is illustrated. As can be seen, the wind farms are situated in areas close to shipping lanes with high-density traffic. It is evident that the risk of colliding with the OWTs exists, and that the extensive development and construction of new sites introduces challenges connected to this. Besides the increase in power capacity of the individual OWTs, the wind farms also show a growing trend in the number of OWTs within each site, according to WindEurope (2020). Each turbine is subject to service and inspections from approaching service vessels, which adds on to the already existing risk of impacts from the commercial traffic lanes.

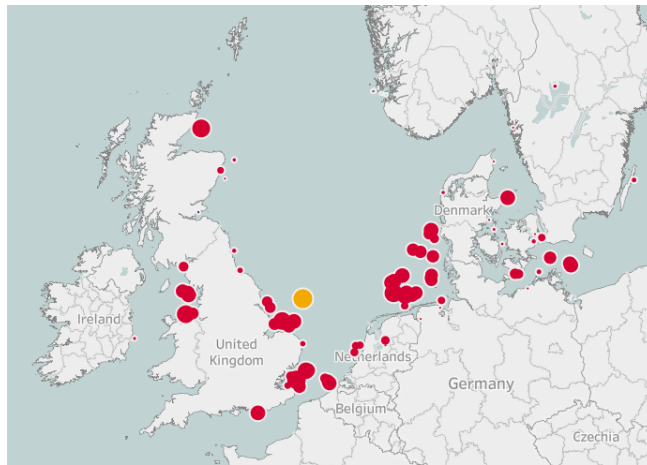


Figure 2.8: Overview of European offshore wind farms as of early 2020. (WindEurope)

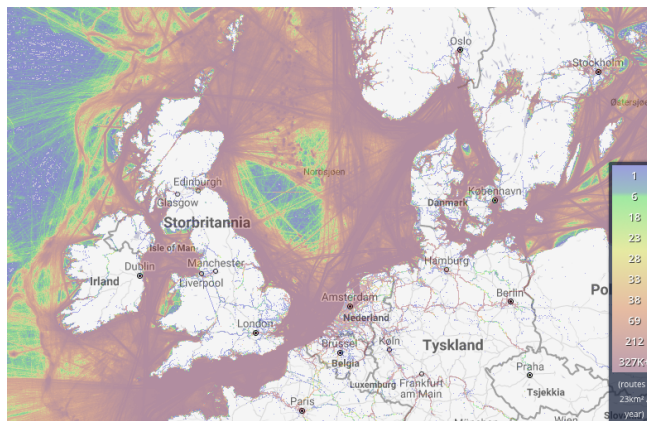


Figure 2.9: Overview of marine traffic density in areas of European offshore wind farms. (Marine-Traffic)

When considering commercial ship traffic and service vessels, several scenarios may occur when it comes to a collision event, and many factors are involved. To mention a few, the ship size, speed, contact location, and contact angle play important roles concerning the consequences. Other aspects like the configuration of the bow and the loading conditions changing the colliding vessel draft will have a considerable influence on the collision event as well. A wide variety of ship types travel in the waters shown in figure 2.9, and the collision events will be highly individual. These factors will be specified for the investigated scenarios later on.

Dai et al. (2013) presents a framework for the analysis of collision risk between service vessels and OWTs. They present the following activities that may lead to a collision event:

- Service vessel approaches an OWT
 - The service vessel fails to stop when it reaches the OWT and collides with the OWT at a high speed
 - Misjudgment of the vessel maneuvering leads to relatively low-speed impact with the OWT
- Service vessel remains alongside the OWT to perform a task, e.g. unloading personnel and equipment
 - Vessel loses power or has a failure in dynamic positioning leading to the vessel drifting into the OWT. Impact speed depends on wind and waves.

The above mentioned activities lead to the following categories for collision scenarios:

1. Head-on collision
2. Maneuvering collision
3. Drifting collision

In the following work, the first scenario of a head-on collision at high speed by an approaching service vessel is investigated.

2.4 Potential consequences

There are different consequences connected to the event of a ship collision, and this must be considered in the design process of the installation. Standards Norway (2004) defines a consequence as "substantial" if the failure event leads to the following three outcomes:

- Danger or loss of human life
- Significant pollution
- Major financial consequences

In the event of a ship collision with an offshore wind turbine, it is evident that the risk of loss of human life is substantially lower than in the case of a collision with an oil platform. This is due to the fact that the wind turbines are generally unmanned except in the case of

service purposes. However, the risks mentioned above still exist as the turbine may fall on the deck of the striking vessel and injure the personnel on board. Also, the impact force of the collapsed turbine may be significant and lead to the rupture of tanks containing hazardous substances causing pollution. Concerning the financial consequences, both damage to the striking vessel and loss of an OWT will have high financial costs from retrieval and repair of damaged property. The event may also cause a temporary shutdown of the wind farm, leading to lost income over time.

For bottom supported offshore wind turbines supported by monopile structures, several potential failure modes are possible, namely:

- Pushover of the support structure, causing the tower and turbine to drop into the sea away from the colliding vessel.
- Collapse of the support structure at the point of impact causing the tower to collapse onto the striking vessel.
- Support structure may resist the impact, but the tower may experience local buckling from the acceleration after impact, causing it to fall onto or away from the vessel.

The collapse mechanisms causing the tower to fall away from the striking vessel are most favorable. This minimizes the risk of causing harm to any person on board the vessel or further damage. However, to design for a favorable collapse mode is challenging as countless variables play a role, and each scenario has to be analyzed separately.

2.4.1 Previous incidents

Even though there are limited numbers of reported collisions with OWTs compared to offshore oil and gas installations, several incidents have happened in recent years. A majority of these incidents include crew transfer vessels (CTVs) used for inspection and service. These have minor collision energy concerning the integrity of the structure, but personnel injuries have occurred. An incident like this happened as recently as the 23rd of April 2020 in the German North Sea, causing three crew injuries (SafetyAtSea.net).

Another recent event with more relevance to this thesis work happened in the Baltic Sea in April 2018. The offshore supply vessel VOS STONE collided with a wind turbine under construction. Both ship and the OWT were damaged, and three crew members suffered minor injuries. The vessel damage was substantial and had to be repaired in a shipyard (Federal Bureau of Maritime Casualty Investigation, 2019). The damage can be seen in figure 2.10.



Figure 2.10: OSV damage after collision with OWT transition piece under construction. (Federal Bureau of Maritime Casualty Investigation, 2019)

A slightly older event from the oil and gas industry is the collision between the well stimulation vessel Big Orange and the Ekofisk platform in 2007. The collision is categorized as a major accident, and both installation and vessel experienced substantial damage. The ship bow was crushed almost 2 meters. The damage can be seen in figure 2.11. The speed of the vessel was approximately 9.3 knots, or 4.8 m/s, at the point of impact and is considered a high energy impact. A collision with a corresponding speed, but with a larger vessel, is investigated later on for the OWT in this work.



Figure 2.11: Big Orange bow damage after collision with water injection platform on the Ekofisk field. (Petroleumstilsynet, 2009)

2.5 Literature study

A literature study of relevant papers and standards has been performed as a first step in solving the thesis's objectives. Topics regarding ship collisions and the offshore wind industry has been of primary focus. Since the offshore wind market has seen rapid development over the last year, this has been important to get an overview of the current state as well as future trends. A lot of work and development have been done within the area of ship collisions during the last decades. Reviewing some of this work has given a good understanding of the problem. The review has also involved collisions with other offshore installations such as jacket platforms, FPSOs, and offshore fish farms. The review will not be given in detail, but a summary of the most relevant and influential literature for this thesis will be given. For more details, reference is made to the original work.

As an introduction to the offshore wind industry in Europe, WindEurope's report on the key trends and statistics for offshore wind in Europe in 2019 gives a broad overview of the industry per today. The report is based on regular surveys of a majority of the companies in the industry, and summarises the construction and financing activities in European offshore wind farms. It also includes an overview of the number of installations, wind farm locations, and governing trends concerning water depths and wind turbine rated capacity. As this thesis mainly focuses on large-volume OWTs with a rated capacity of 10MW and beyond, the key trends in wind turbine size have been especially valuable. (WindEurope, 2020)

Pedersen and Zhang (1998) presented analytical, closed-form expressions for the impact impulse and the energy released for crushing during ship collisions. The analyses done in this paper is restricted to ship motions in the plane of the water surface. The effect of friction is included in their approach; thus the mechanisms of "stick" and "slide" of the colliding bodies are captured. They achieved good agreement with the analytical closed-form expressions, when comparing their results with published results obtained from comprehensive time simulations. Relevant scenarios considered in the article concerning this work include ship-ship collisions, collisions with rigid walls, and collisions with the leg of a jack-up rig.

Liu and Amdahl (2019) presents a new solution to multi-planar impact mechanics for ship collisions. The paper is based on rigid body impact dynamics and handles both planar (3DOF + 3DOF) and multi-planar (6DOF + 6DOF) impacts. A collision matrix relating the ship's main physical and hydrodynamic characteristics for a ship collision is calculated for the first time based on equations of motion and two different coordinate systems. A body-fixed coordinate system with the origin at the center of gravity for each ship is applied, in addition to a local coordinate system with the origin at the point of impact. Closed-form solutions for the dissipated strain energy for the "stick" and "slide" mechanisms are obtained by introducing boundary conditions and friction factors to the problem. The results are also compared to existing and widely used impact mechanics models as the above-mentioned work by Pedersen and Zhang. It is also shown that the method unifies the existing methods for normal direction (Popov et al., 1969), planar space (Pedersen and Zhang, 1998) and multi-planar space (Liu and Amdahl, 2010). This new and advanced solution has not directly been in use in this thesis work as simpler methods have been necessary. However, it has been valuable as it shows the complexity of a ship collision event and the development of the topic in recent years.

Yu and Amdahl (2018) did a review of state-of-the-art response dynamics and mechanics for collisions of tubular structures subjected to ship impacts. Both recent research and classical methods with a broad impact are covered in the paper. This review gave insight and understanding of the impact response of tubular structures and different assessment procedures. It has been beneficial for the further study of the collision scenarios with the OWT. It covers a wide range of the relevant applications studied in this paper, including energy absorption in ship and installation, ship impact loads, global and local response of tubular members, and design considerations to avoid ship impacts.

Ramberg (2011) wrote a master thesis where finite element modelling and simulations of a 500MJ impact between a jacket supported offshore wind turbine and a large oil tanker was considered. Several collapse modes of the installation were investigated by use of the computer program USFOS. It was concluded that the installation was not capable of absorbing and withstanding the design energy. Both favourable and unfavourable collapse mechanisms were found depending on collision scenario. The OWT considered is mounted on a jacket and has considerably smaller dimensions than in this work, but it has been a valuable reference as it considers the same subject and uses the same software.

Chapter 3

Design Principles

This chapter describes the design philosophies that apply to the ship collision scenarios that will be reviewed for the OWTs. A brief introduction to the general requirements for a ship collision assessment will be made. Further on, the concepts of external and internal mechanics, and design methods based on strain-energy dissipation is presented. In addition, the effect of imperfections on the buckling capacity of cylindrical shells is described.

3.1 General

Ship collisions are categorized as accidental loads, and guidance for design and which load effects to consider is given in e.g DNVGL-RP-C204 (DNV GL, 2017) and NORSOK Standard N-004 (Standards Norway, 2004). The standards represent the different limit states to consider in the design, where a limit state represents a condition where the structure is no longer satisfying a targeted safety level. For offshore wind turbines, standards mainly consider four different limit states, namely:

- Ultimate limit state (ULS) - Ultimate resistance of structure for carrying loads
- Accidental limit state (ALS) - Damage due to an accidental event
- Serviceability limit state (SLS) - Exceeding of tolerance criteria for normal use
- Fatigue limit state (FLS) - Failure due to cyclic loads

For this scope of work, the ALS is most relevant and will be discussed further.

The general goal of the accidental load design of a structure is to make sure that the structure's load-bearing function remains intact in the case of an accidental event and that the safety systems remain accessible. Significant damage can be allowed as long as the main safety functions are maintained. According to Standards Norway (2004), this means that the structure during the accident or within a certain time after the accident, shall not impair the following:

- Usability of escape ways
- Integrity of shelter areas
- Global load-bearing capacity

Several accidental loads should be assessed, such as fire loads, explosions, ship impact loads, dropped objects, and abnormal environmental loads, to mention a few. In this thesis, the ship impact loads are mainly focused, with a minor assessment of the effect of earthquake loads.

DNV GL (2017) states that either non-linear dynamic finite element analyses, or energy considerations combined with simple elastic-plastic methods should be used to determine the structural effects from ship collisions. With the computer capacity that is available today, advanced computer analyses have become a preferred tool to assess the collision damage. However, simple calculation models can often be used to verify the integrity of the structure and gives a quick assessment of the problem. Both of these methods are considered in this work.

When investigating the strain energy dissipation in the structure it is also convenient to consider three different levels of the system. According to DNV GL (2017), these levels are :

- A local cross section
- A component or sub-structure
- The total system

The interaction between the different levels shall also be considered.

3.2 Energy formulations

The design ship collision action is characterized by a kinetic energy, which depends on the mass of the ship, the hydrodynamic added mass, and the speed of the ship at impact. According to DNV GL (2017), the design action for fixed installations can be expressed as:

$$E = \frac{1}{2}(m + a) \cdot v^2 \quad \begin{array}{l} m = \textit{ship mass} \\ a = \textit{ship added mass} \\ v = \textit{impact speed} \end{array} \quad (3.1)$$

As mentioned earlier, the different collision scenarios are highly independent. This is reflected by the simple energy formulation above. As the energy is the governing factor of the potential failure modes and consequences, it is clear that any variation that affects either the mass, added mass, or speed will influence the total available energy and create a new scenario of impact. Further on, how the total available energy is distributed between ship and installation during the collision, is highly influential on the response and corresponding potential consequences.

3.2.1 Strength, ductile and shared-energy design

DNV GL (2017) distinguishes between three different design principles with respect to the strain energy dissipation in a collision event. These are:

- Strength design
- Ductility design
- Shared-energy design

The design principles are illustrated in figure 3.1.

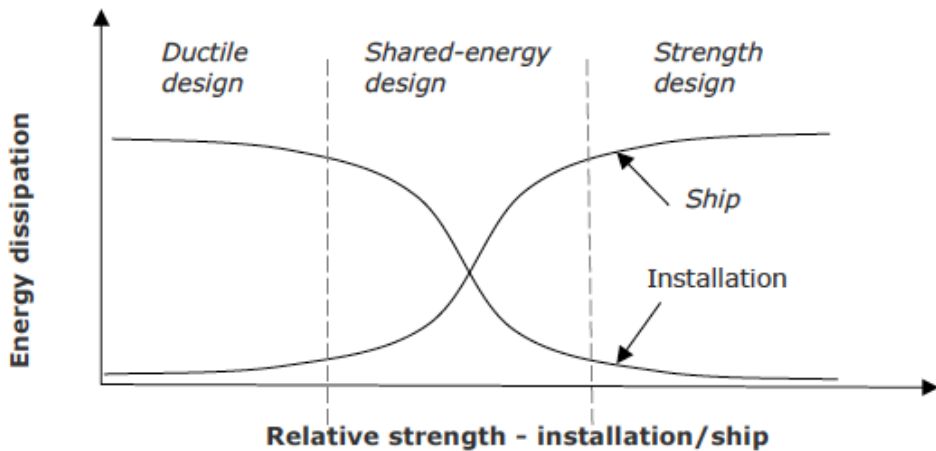


Figure 3.1: Energy dissipation for strength, ductile and shared-energy design (DNV GL, 2017)

In the case of the ductile design, the installation is designed in such a way that it undergoes large, plastic deformations and dissipates the majority of the collision energy. In strength design, the opposite of the ductile design is carried out by making the installation strong enough to resist the impact force with minor deformations. The ship is forced to undergo extensive plastic deformation and thus dissipates the major part of the impact energy. For shared-energy design, the ship and installations are subjected to deformations making them both contribute to the energy dissipation during the impact.

3.2.2 External dynamics and internal mechanics

For the collision scenario the analysis can often be split into two steps:

1. External collision dynamics
2. Internal collision mechanics

The external collision dynamics determines the amount of kinetic energy to be dissipated as strain energy. The energy released from the impact is determined by analyzing the global inertia forces of the striking ship and installation, and taking into account the conservation of momentum and energy. The effect of the surrounding water creating added mass- and viscous forces must also be taken into account. This is the foundation that results in equation 3.1.

The internal collision mechanics deals with the structural response in the collision and determines the amount of energy from the impact that is dissipated in the colliding structures. From this, the distribution of the damage of the two structures can be determined. The structural response of the striking ship and the struck installation can be represented by a load-deformation relationship. This is illustrated in figure 3.2. The total energy dissipation is expressed by the following equation:

$$E_s = E_{s,s} + E_{s,i} = \int_0^{W_{s,max}} R_s dw_s + \int_0^{W_{i,max}} R_i dw_i \quad (3.2)$$

R_s and R_i represents the resistance of the ship and installation, respectively. dw_s and dw_i represents the deformation of the ship and installation.

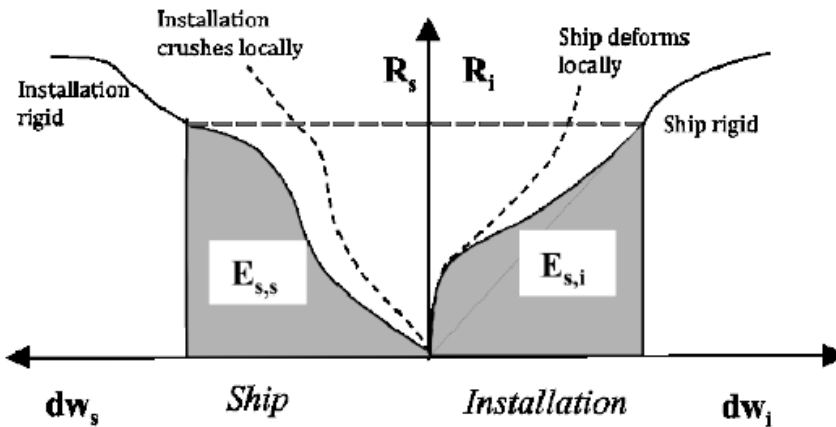


Figure 3.2: Strain energy dissipation in ship and platform during a collision event. (DNV GL, 2017)

It is challenging to obtain the load-deformation relationships, and according to DNV GL (2017) the relationships for the ship and installation are often established independently of each other by assuming the other object infinitely rigid. This will be the case later on in this work. However, these methods may have limitations since both structures will dissipate some energy regardless of the relative strength. For the ship structures, one may often refer to DNVGL-RP-C204 to find recommended force-deformation curves for e.g standard supply vessels of 6500-10000 tonnes. An example of these curves can be seen in figure 3.3. For the installations, the curves will be specific for each case.

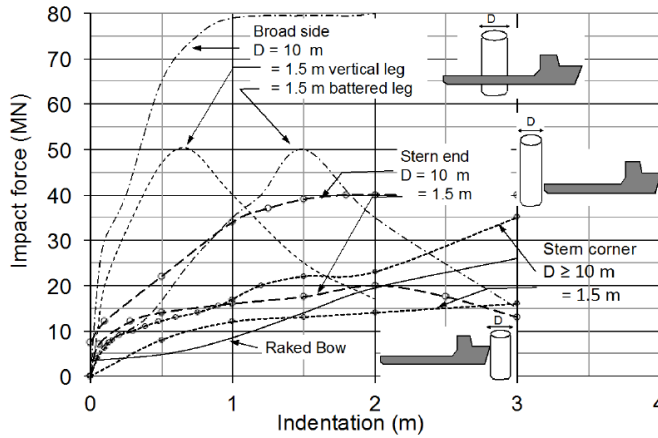


Figure 3.3: Recommended force-deformation curves for beam, bow and stern impacts for standard supply vessels of 6500-10000 tons. (DNV GL, 2017)

The present trend for supply vessels is an increase in size as well as bulbous- and different shapes of the bow, unlike the raked stem or small bulb, as was normal before. These design changes must be considered when using the load-deformation curves. Ice reinforcement will also have a considerable effect on the energy dissipation. An example of a force-displacement curve considering the above-mentioned designs can be seen in figure 3.4. In this work, the force-deformation curves have been obtained for the specific scenarios investigated, using a supply vessel with a bulbous bow. This will be presented later on.

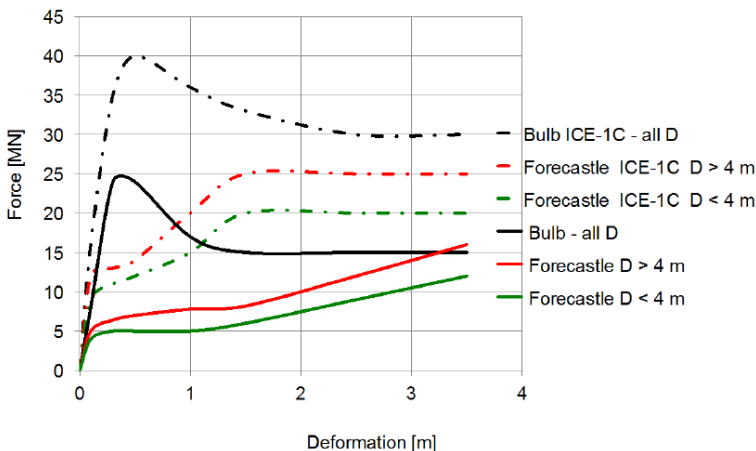


Figure 3.4: Force-deformation relationship for bow impacts from supply vessels with displacement 5-10.000 tonnes - standard bulbous bow with no ice-reinforcement and ICE-1C class. (DNV GL, 2017)

3.2.3 Effect of initial imperfections on the buckling strength of cylindrical shells

The structural model in USFOS described later in chapter 4, is ideal with respect to the structural and material properties. This means that the material is homogeneous, and no out-of-straightness in the structural elements is introduced. In reality, the presence of initial imperfections will always occur due to the nature of manufacturing processes such as welding and rolling of plates. These imperfections have a large influence on the buckling load and must hence be taken into account. In this case, it is especially important, as the buckling behavior of cylindrical shells is usually more violent than it is for plate and column structures.

Basic theory on the topic obtained from Amdahl (2010) is presented to show the effect of imperfections on the buckling behavior of cylindrical shells. Figure 3.5 shows a theoretical load-end shortening curve representative for cylindrical shells subjected to axial compression. The figure shows that during the initial loading, the cylinder follows a stable linear equilibrium curve, before an unstable secondary curve intersects it in point B. The buckling modes are quite different for the deformations in the stable and unstable state. The intersection point B is called the bifurcation point.

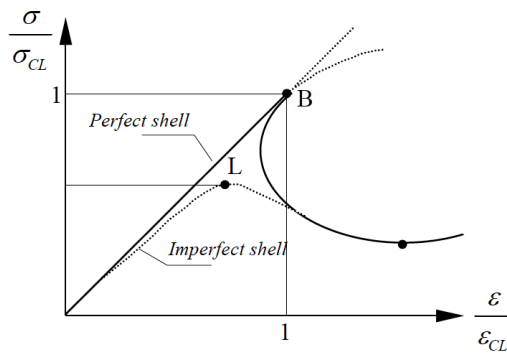


Figure 3.5: Theoretical load-end shortening curve showing equilibrium paths for perfect and imperfect shells subjected to axial compression. B marks the intersection between the stable and unstable state and is called the bifurcation point.(Amdahl, 2010)

As mentioned, the presence of imperfections in real structures is always there to some degree. Thus, the theoretical bifurcation point is difficult to reach in practice. The initial imperfections cause the cylinder to fail at a load level that is significantly lower than the bifurcation load. Thus, buckling will more likely occur at the limit point marked by an L in figure 3.5, rather than at point B.

The influence of the axisymmetric imperfections on the buckling load of an axially loaded cylinder is presented in figure 3.6. The y-axis shows the critical buckling load over the theoretical value, while the x-axis shows the imperfection as an amplitude of the wall thickness.

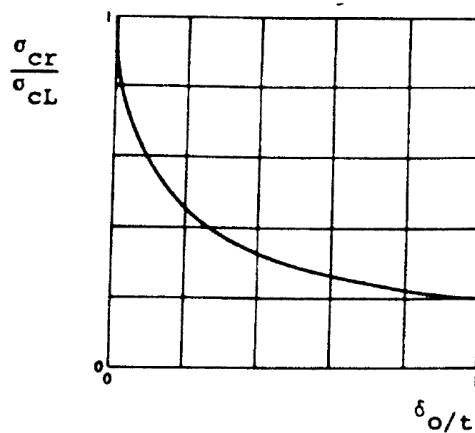


Figure 3.6: Influence of axisymmetric imperfections on the buckling load of an axially loaded cylinder.(Amdahl, 2010)

Figure 3.6 shows that an imperfection of 10% of the wall thickness, results in a substantial reduction on the buckling load to 60% of the theoretical value. Due to the effect of the initial imperfections, the design of cylindrical shells is subject to a reduction of the theoretical buckling load by the so-called knock-down factor to account for this. This will be addressed further in chapter 7 when describing the buckling analysis results.

According to DNV GL (2015) the maximum imperfection for circular cylindrical shells is given by:

$$\delta = \frac{0.01g}{1 + \frac{g}{r}} \tag{3.3}$$

Where g is the length of the rod, and r is the radius of the cylinder, according to figure 3.7.

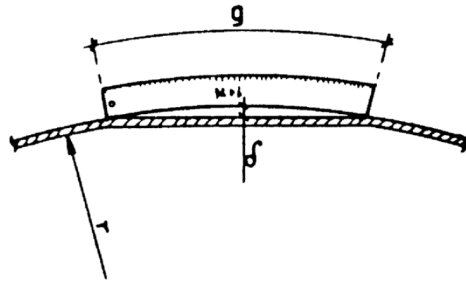


Figure 3.7: Definition of factors used for calculating maximum imperfections in equation 3.3.(DNV GL, 2015)

For the bottom part of the tower, g is equal to 3.26m, and the radius is 4.15m. The maximum imperfection, according to equation 3.3, is then equal to 18mm. In order to trigger the buckling behavior to investigate the potential consequences, a higher imperfection of 40mm is used in this study.

Numerical Modeling of Offshore Wind Turbine, Soil and Loads

The second part of the approach to solve the stated thesis objectives presented in section 1.2 has been to create a representative numerical model to be used in the analyses. In this chapter, the modeling procedure of the OWT model is described. This includes modeling of the blades, tower, support structure, soil- and load conditions. In addition, reference is made to the modeling files attached with this report. These files contain all details regarding the model, and to some extent, comments regarding the different parts that are modeled.

4.1 Reference structure

The offshore wind turbine model created in this work is based on the DTU 10MW Reference Wind Turbine (RWT) by Bak et al. (2013), with some modifications and simplifications. The RWT consists of the tower, blades, and the rotor-nacelle assembly (RNA). With regards to the support structure and soil conditions, information is partly adapted from other previous works, and modified after guidance and approval from the supervisor. The rationale for using the DTU 10MW RWT as a basis for the modeling is that it has a rather traditional design, and a large amount of structural data is openly accessible. This has made the modeling process easier and also provided a basis for comparison and validation of the model along the way.

For a complete overview of the DTU 10MW RWT, reference is made to Bak et al. (2013). Detailed descriptions can be found in the comprehensive data repository that accompanies the report. All properties regarding the blades, RNA, and tower are collected from here if not stated otherwise. The key parameters of the RWT can be seen in figure 4.1.

Parameter	DTU 10MW RWT
Wind Regime	IEC Class 1A
Rotor Orientation	Clockwise rotation - Upwind
Control	Variable Speed Collective Pitch
Cut in wind speed	4 m/s
Cut out wind speed	25 m/s
Rated wind speed	11.4 m/s
Rated power	10 MW
Number of blades	3
Rotor Diameter	178.3 m
Hub Diameter	5.6 m
Hub Height	119.0 m
Drivetrain	Medium Speed, Multiple- Stage Gearbox
Minimum Rotor Speed	6.0 rpm
Maximum Rotor Speed	9.6 rpm
Maximum Generator Speed	480.0 rpm
Gearbox Ratio	50
Maximum Tip Speed	90.0 m/s
Hub Overhang	7.1 m
Shaft Tilt Angle	5.0 deg.
Rotor Precone Angle	-2.5 deg.
Blade Prebend	3.332 m
Rotor Mass	227,962 kg
Nacelle Mass	446,036 kg
Tower Mass	628,442 kg

Figure 4.1: Key parameters of the DTU 10MW Reference Wind Turbine. (Bak et al., 2013)

4.2 USFOS model

4.2.1 Rotor-nacelle assembly modeling

The main characteristics of the RNA are similar to what is used for the DTU 10MW RWT. Detailed modeling of the RNA is not considered as necessary concerning the response of the OWT to ship collision investigated in this work. Thus, the nacelle and hub are represented as nodal masses in the structural model.

The key characteristics of the reference RNA can be found in Table 4.1.

Table 4.1: Main characteristics of RNA. (Bak et al., 2013)

Blade mass	[ton]	42
Hub mass	[ton]	105
Rotor mass (hub + blades)	[ton]	231
Nacelle mass	[ton]	446
Blade length	[m]	89
Hub height over MSL	[m]	119
Hub overhang	[m]	7.1

Due to the absence of the nacelle and hub, the connection between the tower and blades are modeled by very stiff cylindrical members, as the deformations in the hub connection are expected to be minimal. This ensures that the loads are transferred from the blades to the tower without creating abnormal deformations. The blades are first interconnected in the hub center and further connected to the tower by a member extending from the hub center to the tower.

The connection between the blades and tower can be seen in Figure 4.2.

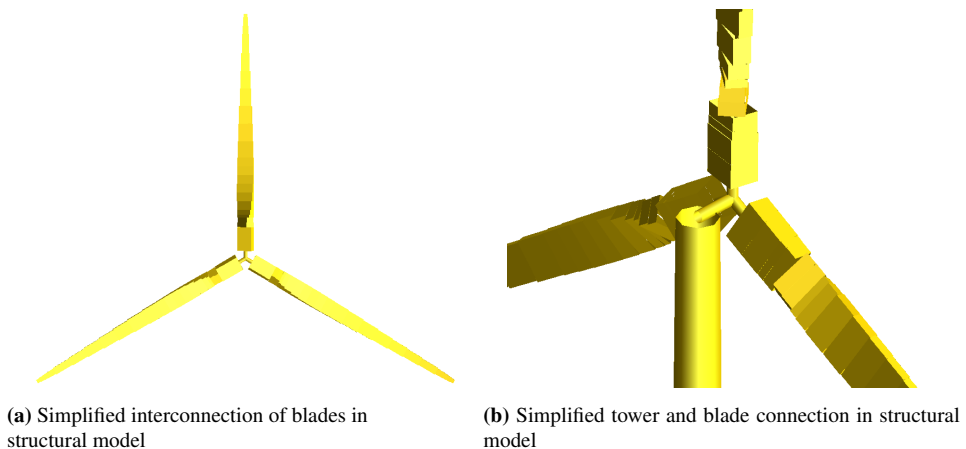


Figure 4.2: Representation of the model simplifications of the RNA and tower-blade connection in USFOS.

The DTU 10MW RWT has a shaft tilt angle of 5 degrees and a hub overhang of 7.1m. This results in a hub height of 119m over the mean sea level (MSL). This can also be seen in Table 4.1. In order to have the ability to rotate the shaft and blades in USFOS easily, the geometry has been simplified by having a horizontal shaft from the tower and neglecting the tilt angle. By neglecting the RNA and the tilt angle, the hub height is reduced by 3.37m. The original hub overhang of 7.1m is defined by the distance along the shaft from the hub center to the yaw axis. The horizontal hub overhang is calculated to be 6.25m, to account for the hub height reduction and removal of tilt. This ensures that the moment arm from the tower to the hub center is retained.

4.2.2 Modeling of blades

As the collision analyses will include the turbine in both parked and operating conditions, a beam model of the blades must be established with the correct flexibility. Especially concerning the operating condition, the inertia effects of the rotating blades are of importance and must be accurately modeled. Details of the aerodynamic design will not be given here. For the detailed design process of the blades, reference is again made to Bak et al. (2013). Briefly explained, the design is based on Blade Element Momentum (BEM) theory with numerical optimization, and is evaluated using Computational Fluid Dynamics (CFD).

The beam model of the blades is generated in USFOS by defining a general cross-section for each blade section to be used in the finite element analyses. Each blade is divided into 26 sections. Input parameters given to each section include the cross-section area, torsion moment of inertia, moment of inertia, plastic torsional section modulus, plastic sectional modulus, and shear area in each direction. The global response of the blades is of interest in this work. To avoid plasticity effects, the yield strength applied for the blades is very high.

Each blade section has different twist angles defined along the blade. As the general beam in USFOS has a circular shape as default, each section is given a box profile simply to get a better visual representation of the geometry and twist of the blades. The blades also have a prebend of 3.3 meters to ensure tower clearance. For the RWT, the tower clearance is 18.26m without loads when including tilt, cone, and prebend of the blades. Due to the simplifications of the RNA described above, the tilt and cone are neglected. This makes the tower clearance considerable less in the model than for the RWT. The clearance will be taken into account when post-processing the results in chapter 6. The beam model can be seen in figure 4.3.

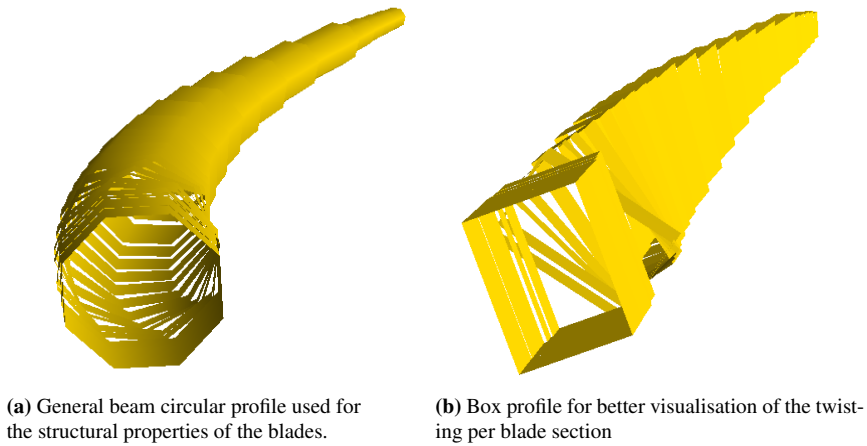


Figure 4.3: Beam model of OWT blades in USFOS representing structural and visual properties.

An eigenvalue analysis is conducted to compare the natural frequencies with the reference model, in order to validate the established blade model. The results can be seen in Table 4.2. As can be seen, there is good correspondence between the lower modes but an increasing difference for the higher modes. As the lower modes are considered most important in this work, this is considered acceptable. The higher modes are of less importance concerning the ship collision response.

Table 4.2: Comparison of natural frequencies of isolated blades between model and the reference wind turbine of Bak et al. (2013).

Mode	RWT	USFOS	Difference [%]
	f_n [Hz]	f_n [Hz]	
1st flap mode	0.61	0.61	0.00
1st edge mode	0.93	0.91	1.85
2nd flap mode	1.74	1.82	4.58
2nd edge mode	2.76	2.92	5.35
3rd flap mode	3.57	3.89	8.23
4th flap mode	6.11	6.82	10.46
3rd edge mode	6.66	6.27	6.15

4.2.3 Tower modeling

The tower used in this work differs slightly from the DTU 10MW RWT. The reference turbine does not include any support structure or soil, which in contrast, is introduced here. The tower thickness is increased by 20% as described in Bachynski and Ormberg (2015), to have a realistic tower which is not too soft compared to the stiffer supporting structure. This is also done for comparison purposes as the monopile structure introduced further on is based on Horn (2018). The model used in that work also implements the same increase in tower thickness. With the exception of the changes in tower thickness, the main dimensions remain identical to the RWT and are presented in table 4.3.

Table 4.3: Main characteristic dimensions of the OWT tower.

Tower height	[m]	116
Tower overall mass	[ton]	628
Tower outer diameter (top to bottom)	[m]	5.5-8.3
Tower thickness (top to bottom)	[mm]	24-46
Material density	[kg/m ³]	8500

The tower material is steel, but as can be seen in table 4.3, the density is slightly higher than the actual density of steel. The reasoning behind this is to account for some secondary structures in the tower, according to Bak et al. (2013). The tower model, together with the attached blades and nodal masses, represents the wind turbine. The wind turbine is illustrated in figure 4.4.

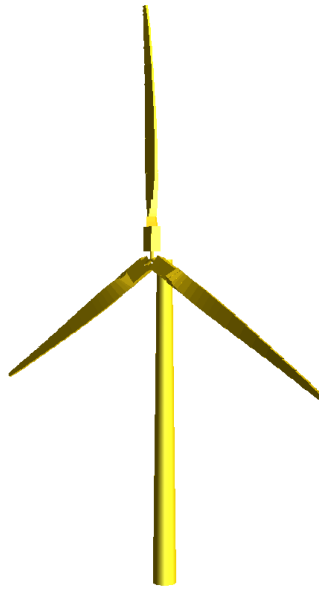


Figure 4.4: Complete structural model of OWT including the tower, RNA and blades.

4.2.4 Modeling of monopile foundation

The wind turbine model described so far is to be investigated mounted on an XL monopile. The dimensions of the monopile are obtained from Horn (2018), and is based on a preliminary design performed by Velarde (2016) at NTNU. It consists of a 20-meter transition piece which spans from 10 meters below the mean sea level (MSL), and up to the tower base at 10 meters above the MSL. From the transition piece, the monopile continues to the seabed, which is located at a depth of 30 meters. Finally, the monopile penetrates 42 meters into the soil. The diameter of both the transition piece and monopile is 9 meters, while the thickness is 150 and 110 mm for the transition piece and monopile, respectively.

The model uses an extended pile model in USFOS, made available as recent as late 2019. USFOS originally is a tool tailor-made for jacket structures, where the foundation typically consists of a series of single slender piles connected to the legs. USFOS (2019) states that the original pile model cannot describe the global bending moment resistance correctly. If a jacket pile model had been used to represent the monopile, the global bending resistance would have been underestimated. This is mainly due to the large dimensions of the monopile, which has a larger friction area, which in turn provides an additional bending resistance compared to the smaller piles used for jackets. Thus, the extended pile model has been used in this work.

According to USFOS (2019), the extended monopile model in USFOS represents the structure by using discrete integration points along the circumference. Each integration point represent a certain arc of the monopile, where the integration point area, dA , becomes:

$$dA = \alpha \cdot R \cdot t, \quad \text{where} \quad \alpha = \frac{2\pi}{n} \quad (4.1)$$

n is the number of integration points. Each integration point will have a contribution, dM , to the total bending resistance equal to:

$$dM = dA \cdot \sigma \cdot r \quad (4.2)$$

where r is the distance to the actual rotation axis and σ is the stress in the actual integration point. The product of dA and σ is the integration point force, dF , and the moment can then be written as:

$$dM = dF \cdot r \quad (4.3)$$

This integration point technique is used when modeling the monopile, and the concept is visualized in figure 4.5.

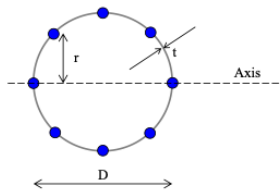


Figure 4.5: Pipe with 8 integration points along the circumferential. (USFOS, 2019)

The actual pile in this case is modeled by 16 integration points - or auxiliary piles - located along the real monopile's circumference. These auxiliary piles represent the monopile resistance, and the forces occurring in each single pile is transferred to the monopile. The monopile model can be seen in figure 4.6, including the auxiliary piles. The soil layers can also be seen, and is described in the following.

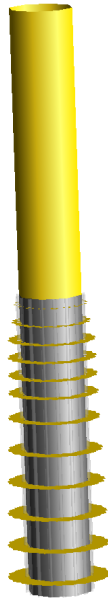


Figure 4.6: Generated monopile model including representation of the soil layers.

4.2.5 Modeling of soil conditions

Geo-technical design and the procedures for generating soil models are complicated and an own field of research. Only a brief description will be given here. The soil model used in this work is adapted from Smilden et al. (2020) with some modifications. This random field model is based on a wind farm site at the Dogger Bank in the North Sea. For a detailed description of the soil model generation procedure, reference is made to the original work.

Soil characteristics have a large influence on the OWT structural response as it affects both the stiffness and damping of the system, as well as the boundary conditions applied at the soil-structure interaction. At the same time, the soil is one of the primary sources of uncertainties in the modeling process. One reason comes from the nature of the soil, as it is a heterogeneous material with a wide variety of properties. The soil materials can vary between everything from soft sand to stiff clay, depending on the location of the site. Smilden et al. (2020) states that: "the inherent soil variability is usually modeled as random fields characterized by their mean, coefficient of variation (COV), and scale of fluctuation." An illustration of this can be seen in figure 4.7.

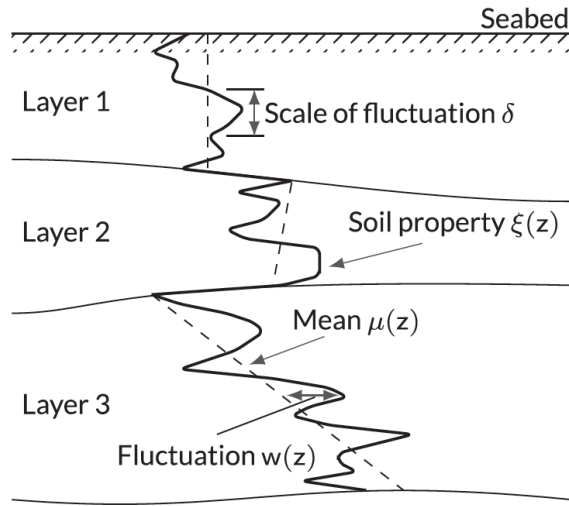


Figure 4.7: Random field model of soil including sources of uncertainty. (Smilden et al., 2020)(adapted from Phoon and Kulhawy (1999))

A simple three-layered soil model is constructed based on the soil conditions of the Dogger Bank wind farm site. The soil consists of a dense layer of sand at the surface, followed by layers of stiff clay underneath. The model properties are shown in figure 4.8.

Layer	Depth Range, m	Type	Soil Property	Distribution	Mean $\mu(z)$	COV, %	Scale of Fluctuation δ , m
1	0-5	Dense sand	Friction angle ϕ , deg	Normal	40	15	0.5/2.0/5.0
			Submerged unit weight γ , kN/m ³	Deterministic	10	0	∞
2	5-15	Stiff clay	Undrained shear strength s_u , kPa	Lognormal	75	40	1.0/5.0/10.0
			Submerged unit weight γ , kN/m ³	Deterministic	10	0	∞
3	15-38	Stiff clay	Undrained shear strength s_u , kPa	Lognormal	$75 + 3(z - 15)$	40	1.0/5.0/10.0
			Submerged unit weight γ , kN/m ³	Deterministic	10	0	∞

Figure 4.8: Three-layered field model properties applied to soil model in USFOS. (Smilden et al., 2020)

For this work, the mean values in the table are used to construct the layers. Note that the random field model only covers a depth range of 38 meters, while the monopile model goes 42 meters into the ground. This is solved by extrapolating the values for the remaining 4 meters. In addition, the shear strength is increased to lower the natural period in fore-aft and side-side motion. By doing this, resonance occurring when coinciding with the blade passing frequencies is avoided. The lowest blade passing frequency, 1P, corresponds to a period of 6.25s, which is close to the natural periods of the first mode of the tower.

The soil characteristics are implemented in the USFOS model by using nonlinear springs. Each spring is visualized as a disk, where each represents the relative strength of the actual layer. Stronger layers are represented by proportionally larger diameter disks. This can also be seen in figure 4.6, as the weak upper sand layers are represented by smaller disks than the stiff clay layers further down on the monopile. The soil curves for each layer are automatically generated by a built-in command in USFOS, which uses the recommended practice by the American Petroleum Institute (API) (2011).

In figure 4.9, the soil plastic utilization under the operational condition is presented. It can be seen that the upper sand layers are highly utilized when the self-weight and loads are applied.

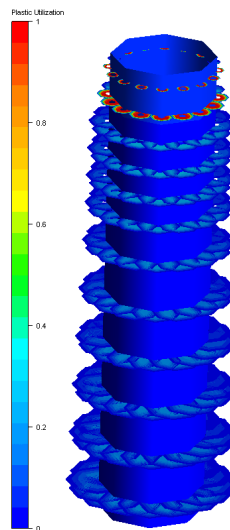


Figure 4.9: Soil utilization of OWT while in operating condition with applied wind loads.

A comparison between the natural periods of the monopile-mounted OWT of Horn (2018) has been made to validate the monopile model and the soil characteristics applied. This model has similar dimensions and soil conditions and acts as a good basis for comparison. The results are presented in table 4.4. The models show good correspondence with only a small difference in the 1st modes of the side-side and fore-aft motion.

Table 4.4: Comparison of natural periods between monopile-mounted OWT model and similar model of Horn (2018).

Mode	Horn	Model	Difference [%]
	T_n [s]	T_n [s]	
1st side-side	4.6	4.7	2.2
2nd side-side	0.9	0.9	0.0
1st fore-aft	4.6	4.7	2.2
2nd fore-aft	0.9	0.9	0.0

The modes corresponding to the different natural frequencies can be seen in figure 4.10.

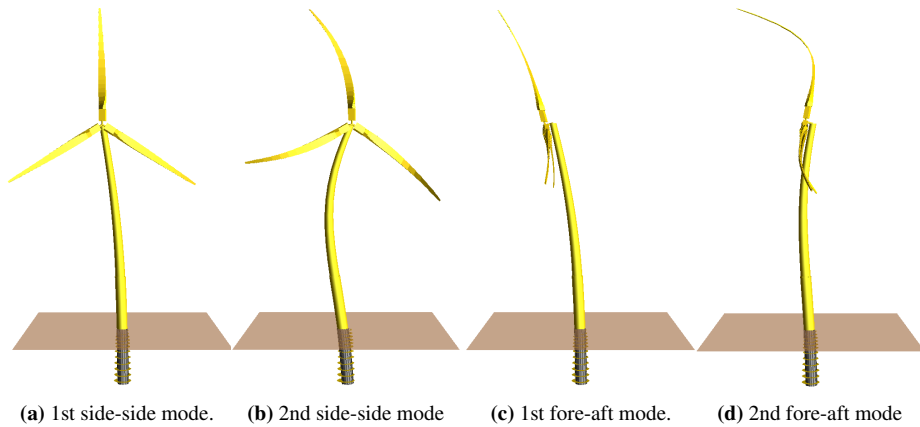


Figure 4.10: Vibrational modes of monopile-mounted OWT model. Scaled up for visualisation purposes. Soil is included.

4.2.6 Modeling of applied loads

The applied loads on the structure mainly consist of the gravitational loads on the body, the torque rotating the blades, and the associated blade loads generated from the wind. The collision and earthquake loads will be described separately. The effect of wave loads is not considered in this work, but a "dummy wave" is applied with zero wave height to represent the sea surface.

Since the effects of the inertia forces of the rotating blades are of interest, the maximum rotor speed has been chosen to include the largest effects. From figure 4.1 this is given as 9.6rpm, which is equivalent to 1rad/s. The rotational speed is achieved by gradually applying a torque load to the node connecting all the blades. The parked OWT is loaded over a period of approximately 40 seconds before it reaches the maximum speed. This is illustrated in figure 4.11.

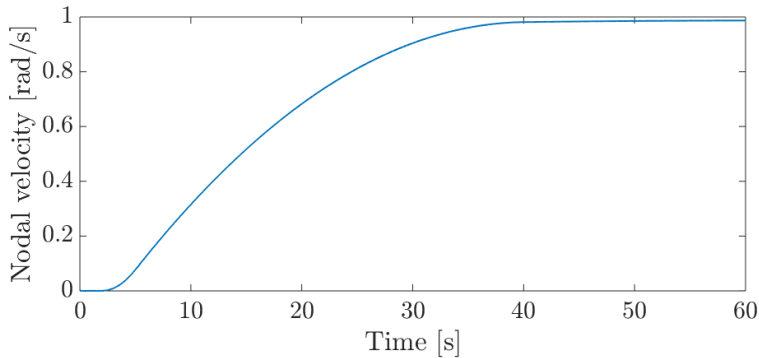


Figure 4.11: Gradual increase of the rotational speed of the OWT blades in operating condition.

The nature of wind loads are highly dynamic, and dedicated computer programs are necessary to calculate them. Since this work mainly considers accidental loads, the need for a highly detailed wind load model has not been considered as essential. However, a part of the thesis objectives have been to investigate the effect of the operational condition on the ship collision response of the OWT. Thus, it has been necessary to establish a simplified model to assess these loads. The process of creating the simplified wind loading model has been rather extensive. The calculations are done by using Microsoft Excel and the data repository attached to the report by Bak et al. (2013). An outline of the process will be described in the following.

As mentioned in section 4.2.2, each blade is divided into 26 different sections with different foil profiles and structural properties. When the rotor is running, the blades are exposed to an incoming flow of air, both from the wind and the rotational speed. Depending on several factors such as the rotational speed, wind speed, foil shape and blade twist, each section of the blades will generate a lift- and drag force of some magnitude. An illustration of the forces experienced by a wind turbine blade section can be seen in figure 4.12.

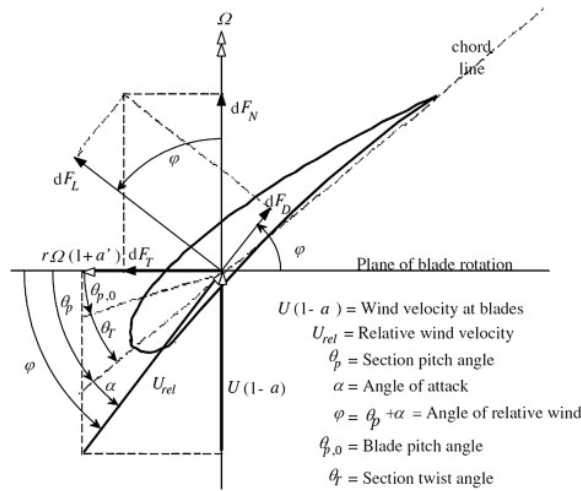


Figure 4.12: Blade forces on a foil cross section of a wind turbine blade. (Manwell et al., 2010)

The lift and drag forces on each blade section are calculated from equation 4.4 and 4.5 respectively.

$$F_L = \frac{1}{2} \rho v^2 C_L A \quad (4.4)$$

$$F_D = \frac{1}{2} \rho v^2 C_D A \quad (4.5)$$

Where F_L and F_D are the lift- and drag force for each section, respectively. ρ is the density of the air, v is the relative wind velocity at the blades, C_L and C_D are respectively the lift- and drag coefficients and A is the planform (projected) wing area. The value of ρ in the calculations is set to $1.2 \frac{kg}{m^3}$. Values for the coefficients and the dimensions needed to calculate the planform area is found in the data repository in Bak et al. (2013).

The force is calculated over the projected length of the sections to obtain the total force over the blades. Finally, the loading condition is simplified by distributing the total load as point loads in the center of each blade section.

The nodal loads have been simplified further only to contain the component in the wind direction corresponding to the global y-direction in the model. These are the most crucial load components in this context, as it affects the global bending moment of the OWT. The force components in the global z-direction, i.e. towards the seabed, are small compared to

the forces originating from the self-weight and the nodal masses representing the RNA at the tower top. These are disregarded in the analyses.

Due to the presence of the turbine, some of the incoming wind will be deflected away from the turbine. This causes the air passing through the blade disk to have a smaller velocity than the free-flowing upwind air. This results in smaller generated loads which are taken into account. The ratio describing this reduction of the wind speed at the rotor is called the axial induction factor, a . This factor is described by:

$$a_i = \frac{U_1 - U_2}{U_1} \quad (4.6)$$

Where U_1 is the wind speed far upstream of the turbine, and U_2 is the wind speed at the rotor blades. After cooperation with the supervisor, it was decided to simply reduce the total calculated wind loads by a factor of 0.3 to account for this effect. A visualization of the complete model with the applied nodal loads can be seen in figure 4.13.

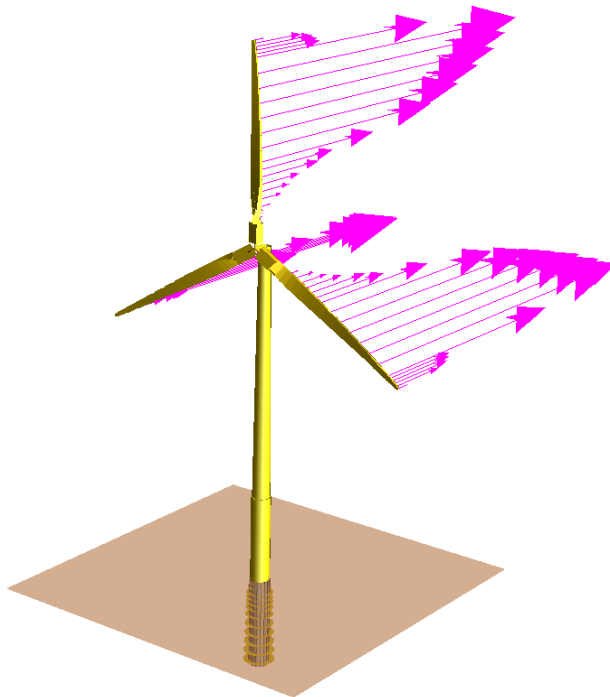


Figure 4.13: Simplified wind load model representing the distribution and magnitude of nodal loads applied along the OWT blades.

4.2.7 Ship impact modeling

The collision scenarios in this thesis consist of head-on collisions with the OWT, acting in the opposite direction of the wind. The collision is centric, meaning that both mass centers of the ship and installation lies in the line of impact. This is expected to give the most unfavorable and conservative collision event. The striking ship is an offshore supply vessel with a bulbous bow, and the impact occurs at the transition piece of the OWT.

Two impact points are defined on the transition piece, namely one corresponding to the center of the bulb and one in the bow superstructure. The bulb impact point is located 3 meters below the free surface, while the bow superstructure point is located 5 meters above the free surface. As the bow protrudes 1.2 meters in front of the bulb, the bulb spring is not activated before the bow is crushed this distance.

The displacement of the ship is 7500 tons, and a constant added mass of 10% is utilized for the bow collision event. The collision scenarios include analyses of the turbine in both parked and operational conditions, to investigate the effects the inertia forces may have on the response. Two different ship velocities are considered: 3m/s and 5m/s. By application of equation 3.1 these velocities result in collision energies of respectively 37MJ and 103MJ. The latter velocity can be compared to the like of the Big Orange impact on Ekofisk mentioned earlier in section 2.4.1. However, the supply vessel considered here is considerably larger.

The impact modeling is divided into two parts, namely:

1. Local analysis of ship impact in LS-DYNA to retrieve force-deformation curves
2. Implementation of force-deformation curves in USFOS

The modeling description of part 1 will be described separately in section 4.3.

The impact is modeled in USFOS by the use of a spring system, as shown in figure 4.14. It includes two nonlinear springs and two linear springs which are attached to the transition piece. The elements 10110 and 10210 are linear, while 10120 and 10220 are nonlinear springs. The upper part represents the forecastle, and the lower part represents the bulb of the supply vessel. At the end of the springs, a vertical column is attached. This column has a concentrated mass of 8250 tons, and represents the ship- and added mass. This column is given the velocity of the actual collision events when performing the analyses.

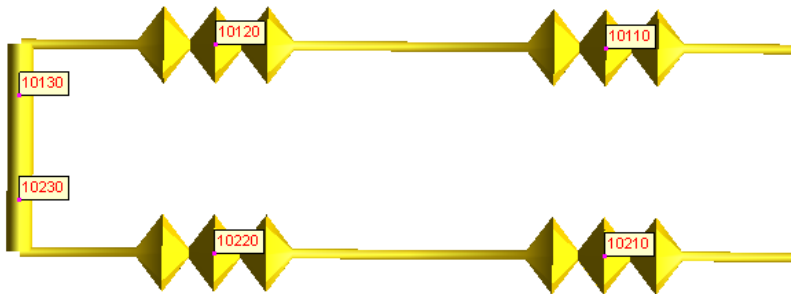


Figure 4.14: Spring system representing the force-deformation curves applied in the collision analysis in USFOS, with column representing ship mass and added mass.

The nonlinear springs are used to represent the true stiffness of the ship at the contact points. The analysis of the crushing procedure is extensive and demands a very high computational capacity to carry out. Due to this, the crushing analysis is performed separately and then implemented as force-deformation curves in the nonlinear springs. The separation simplifies the global USFOS analysis and saves a lot of computational time.

The force-deformation curves used as input to the nonlinear springs are obtained by crushing the bow at a constant speed into the cylinder. Thus, something is needed to model the resistance during the collision. The linear springs serve this purpose as they are used to model the ship offloading after the impact. These springs have zero stiffness in tension and 100MN/m in compression. The effect of these springs will be shown later when describing the collision analyses.

4.2.8 Modeling of earthquake

This thesis mainly considers ship collisions with the OWT. However, when modeling the wind turbine, the idea of running an earthquake analysis to test the performance of the OWT was found interesting after guidance from the supervisor. Several of the vibrational modes from the validation of the structural model was found to be interesting with respect to potential earthquake loads. It must be mentioned that the soil characteristics applied in this work are based on the Dogger Bank, which is located in the North Sea. This area has a low occurrence of earthquakes. However, OWTs of the dimensions used in this work will be constructed in areas where the occurrence of earthquakes is higher. Even though the soil conditions may be different, it was decided to create a simple earthquake model to be applied to the structure to investigate the OWT response and potential failure modes.

The earthquake is applied to the structural model by prescribed displacements in the soil, through a built-in command in USFOS called SOILDISP. This command takes into account the interaction between the soil and structure through the nonlinear springs representing the soil layers. Based on the stiffness of the soil layers, the soil displacements are then transferred to displacements of the monopile structure.

The load history applied in this work was given by the supervisor and is based on the 1952 Kern County earthquake in California. The displacement history given has a duration of 60 seconds and can be seen in figure 4.15.

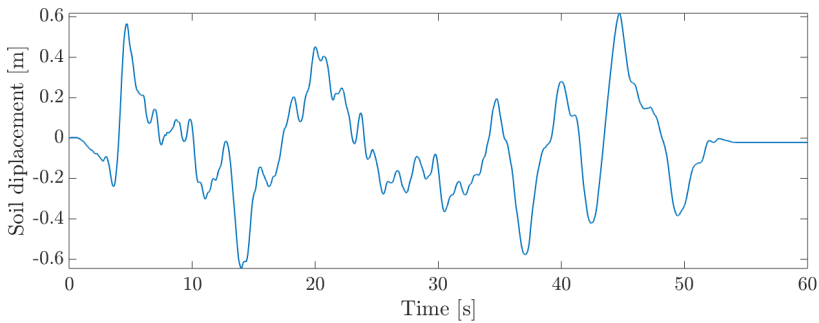


Figure 4.15: Soil displacement history applied in earthquake analysis on OWT.

It can be seen that the maximum displacement is approximately 0.6 meters in each direction, resulting in a total displacement of 1.2 meters. The soil displacements are applied separately for the global x-direction (blade direction) and y-direction (wind direction) to observe which are more critical. Besides, the displacements are scaled up to investigate the effects of potential larger earthquakes on the buckling response described in chapter 7.

4.2.9 Shell modeling of bottom and midsection of tower

The investigation of possible local buckling of the tower requires that the critical sections are modeled with shell elements to capture the local effects. Critical means that structural members have a high utilization factor with respect to their buckling capacity. This will be described in more detail later on. The critical sections for the ship impact and earthquake events were found by investigating the results from the global analyses of the beam model in USFOS. The critical sections for the ship impact and earthquake were found to be respectively the bottom and middle part of the OWT tower.

Subsequently, these two parts were isolated from the beam model and converted into shell

elements for the buckling analyses. A built-in function in USFOS named SUBSHELL was used to create the shell elements. This record lets the user specify the beam element, and then automatically generates a shell model that replaces the original beam element in the model. The beam element properties are transferred to the shell element.

The mesh density of the beam element is conducted by another built-in function named MESHPIPE. The function generates the mesh for the selected element by specifying the number of shell elements in the longitudinal and circumferential direction. Due to computational capacity limits, a relatively coarse mesh of 20x20cm is used for the buckling analyses. This mesh size obtained reasonable computational times, and at the same time, captured the local effects of buckling. Both the bottom and mid-section of the tower is 5m long. The shell representation of the bottom part of the tower is shown in figure 4.16. An equivalent model is made for the mid-section.

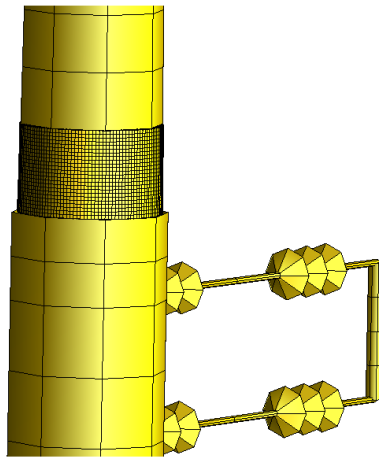
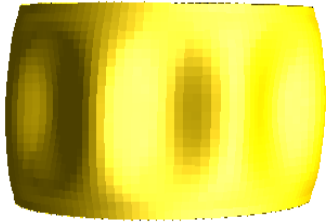


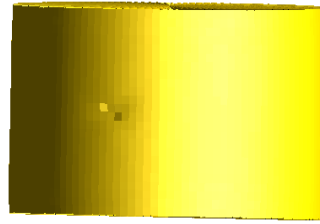
Figure 4.16: Shell representation of the bottom part of the OWT tower with mesh, used in the buckling analysis when subjected to ship impact.

The imperfections in this work are mainly added by using an in-built function in USFOS called BUCKMODE. This function performs an eigenvalue analysis of the model, and applies the initial imperfections as a scale of the eigenmode by adding them to the initial nodal coordinates of the structure. Also, the effect of denting is investigated to some extent by the use of the in-built function GIMPER, which adds a user-defined dent. The models for adding the imperfections to the shell sections are visualized in figure 4.17. Due to the coarse mesh, the figures are slightly difficult to see, but the eigenmodes and dent have been

presented to the best of their ability.



(a) BUCKMODE, representing imperfections by eigenvalue considerations.



(b) GIMPER, representing imperfections in form of dent in the structure.

Figure 4.17: Visual representation of the two different models used for introducing initial imperfections in the tower in the structural model. Up-scaled for visual purposes.

4.3 LS-DYNA model

4.3.1 Ship modeling for local analysis

In this work, a supply vessel with 7500 tons displacement and a bulbous bow is used. A finite element model of the impacting ship was made available by the supervisor. For the sake of the collision analysis, only the bulkhead part, including the bulbous bow, is modeled in detail. The finite element model can be seen in figure 4.18.

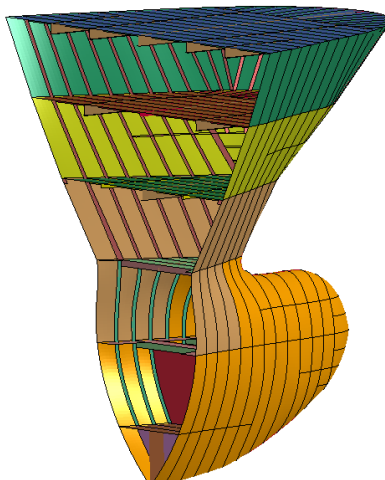


Figure 4.18: Finite element model of supply vessel bow used in bow crushing analysis in LS-DYNA.

The main dimensions of the bow section model consist of the length, height, and width. These are respectively 9.6m, 15.7m, and 16.1m. The draught of the ship is 6.2m. The bow section finite element model consists of 67872 4-noded shell elements, which include membrane, bending, and shear deformation. The default shell in LS-DYNA applies the Belytschko-Tsay formulation. The thickness varies from 7mm (deck plating) to 20mm (bulb center plate). The general size of the elements is 120x120mm. The material used is ordinary steel. The bow is 1.2m ahead of the bulb tip. Thus, the bow will experience extensive damage before the crushing of the bulb is commenced. This is accounted for in the spring system representation in USFOS.

The contact points in the spring model representation corresponds to the tip of the bulb and a point at the forecastle with height equal to the second-highest deck. This point is chosen lower than the bow tip because the highest initial force occurs after some deformation of the bow, as seen in figure 5.3. The ship section is fixed in all directions at the boundaries of the rear part.

4.3.2 Modeling of transition piece for local analysis

The transition piece used in the global analysis in USFOS is a basic column with a length of 20m and a thickness of 150mm. Due to these solid dimensions, it is expected that the ship will experience the majority of damage during impact, while the local damage will be small for the transition piece. Due to this and for simplicity, the column is modeled as a rigid body. Since the collision is further simplified to be represented by nonlinear springs at two contact points, the column model is divided into two equal parts. This way, the force-deformation curves for the forecastle and bulb are obtained individually. Instead of moving the ship section, the column is given a prescribed motion while the ship section is fixed. An illustration of the model of the forecastle analysis is presented in figure 4.19. An equivalent model for the crushing of the bulb is made as well, and is illustrated in figure 4.20.

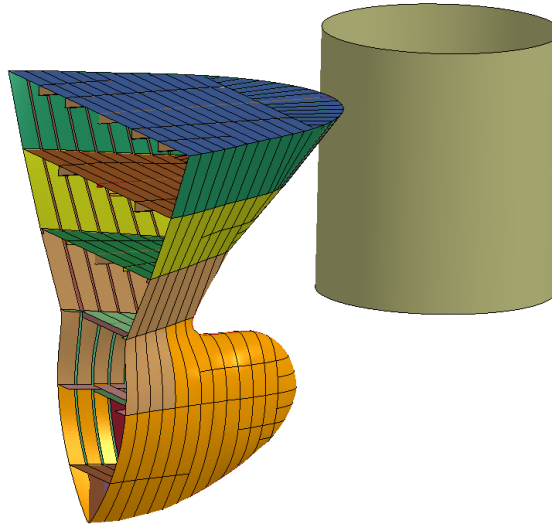


Figure 4.19: Finite element model of supply vessel bow and rigid cylinder for obtaining force-deformation curves for forecastle.

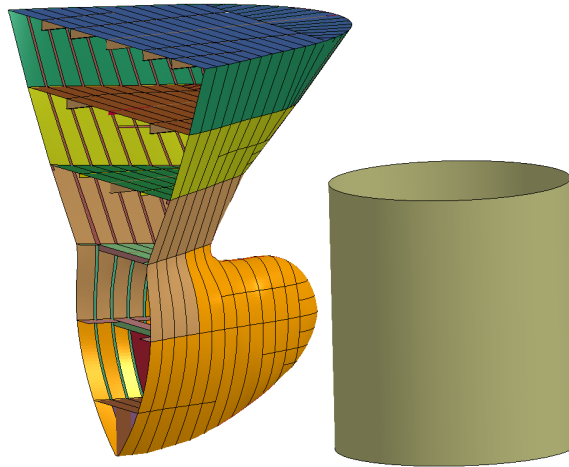


Figure 4.20: Finite element model of supply vessel bow and rigid cylinder for obtaining force-deformation curves for bulb.

Chapter 5

Local Analysis of Bow Crushing in LS-DYNA

The ship collision analysis is split into two sub-tasks, where the first part consists of a local review of the bow crushing of the supply vessel described in section 4.3.1. The local analysis is done using the computer program LS-DYNA, which performs nonlinear dynamic finite element analysis using explicit time integration. This analysis computes the relative strength and deformation of the ship, when subjected to an impact with the transition piece.

The primary purpose of the analysis is to obtain the force-deformation curves for the bow section. These curves are further used to define the nonlinear springs used to represent the collision event in the global analysis in USFOS, as described in section 4.2.7. The force-deformation curves are of importance as it determines the level of energy in the ship collision event.

The analysis is carried out by fixing the modeled ship section, while moving the fixed cylinder representing the transition piece towards the structure at a constant speed of 3m/s. The chosen velocity has no other purpose than achieving reasonable computational times. The actual ship collision speed is applied in the global analysis. Self-contact between the internal structural components of the bow is accounted for during the collision analysis. Master-slave contacts are also defined between the column and the bow and bulb.

The computational capacity required to conduct these analyses is significant, and would by use of a regular computer, take several days and up to weeks to perform. Due to this, it was granted computational time at one of the super-computers at NTNU, called Vilje. This reduced the original computational time of several days, down to a few hours.

An illustration of the bow and bulb before and after the impact can be seen respectively in figure 5.1 and figure 5.2.

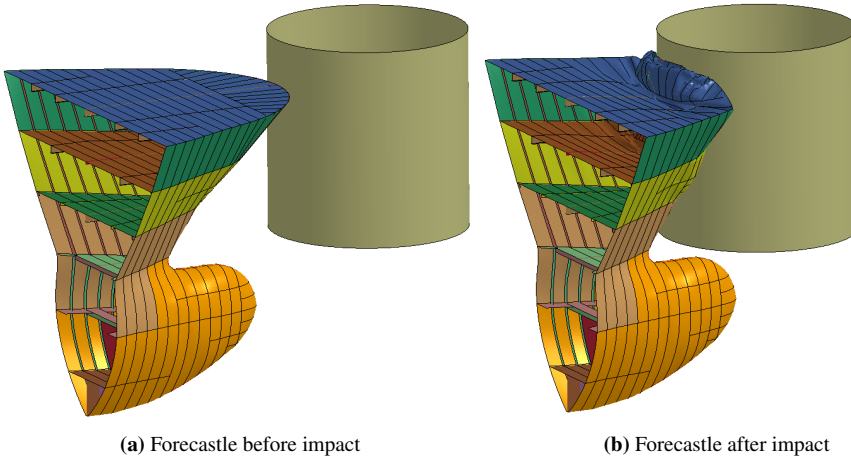


Figure 5.1: Deformation of the forecastle before and after the crushing analysis.

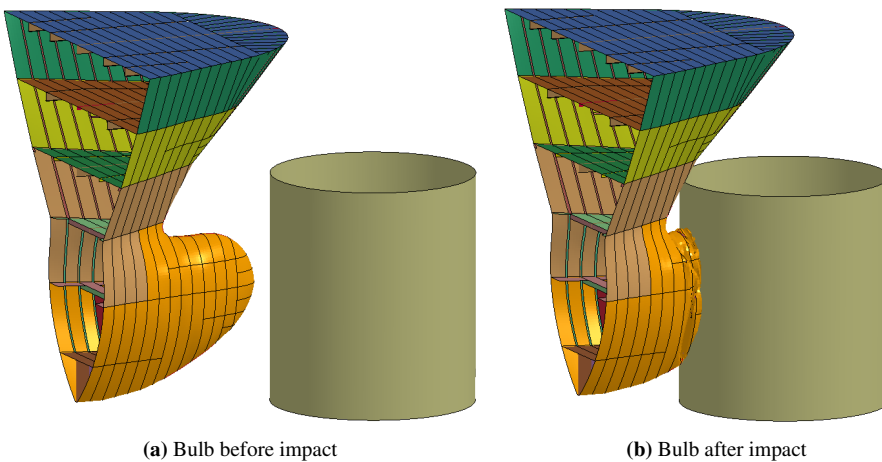


Figure 5.2: Deformation of the bulb before and after the crushing analysis.

The force-deformation curves obtained in the crushing analysis in LS-DYNA for the forecastle and bulb can be seen in figure 5.3.

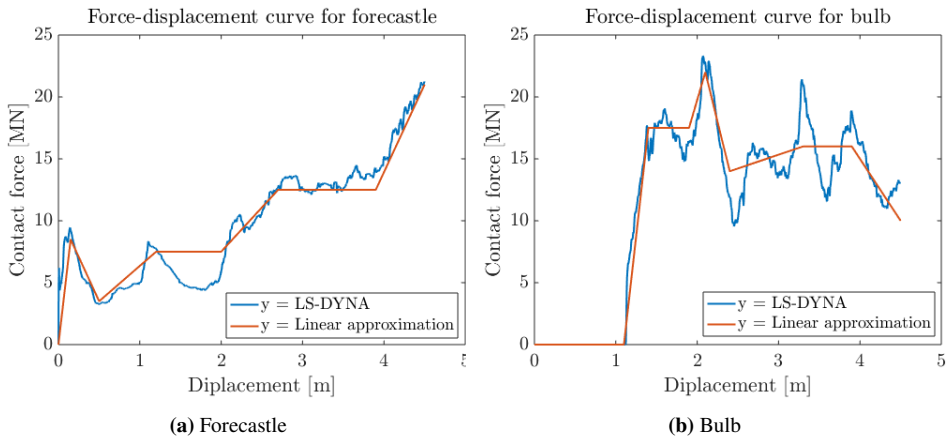


Figure 5.3: Force-deformation curves for forecastle and bulb obtained from bow crushing analysis in LS-DYNA. Linear approximation to be applied in global USFOS analysis is included.

The curves represent that the forecastle protrudes 1.2m in front of the bulb tip as the bulb obtains no force before the forecastle is deformed this distance. It can be seen from the figures that the force for both the forecastle and bulb initially obtains a peak after a small amount of deformation. This is mainly due to the rapid increase in the contact area between the colliding structures. At the initial contact point, the area is small. When the rigid cylinder moves further through the ship sections, the area increases, leading to an increased contact force.

The contact areas also describe the trend of the figures as the contact force of the forecastle gradually increases with increasing deformation, while the bulb remains at a more constant level. This is natural if one takes a look at the geometry of the forecastle and bulb. The forecastle develops a much wider area when moving from the bow tip and inwards. The bulb cross-section, on the other hand, changes less relative to the bow. This leads to less increase in the contact area.

Further on, the peaks can also be described by looking at the ship geometry and the structural properties of the stiffening elements. The force-deformation curves for the forecastle obtain peaks at approximately 1.2m and 2.2m deformation. The peaks occur due to the activation of the main stiffeners of the skin plates as well as the second deck from the top. These members are relatively stiff and add on to the total stiffness of the system be-

ing crushed. This is reflected as a steep increase in the force-deformation curves, since the slope represents the stiffness. Equivalent to the forecastle, the peaks obtained for the bulb also is a result of the activation of stiff members such as the ring frames. The main stiffening elements of the ship are shown in figure 5.4.

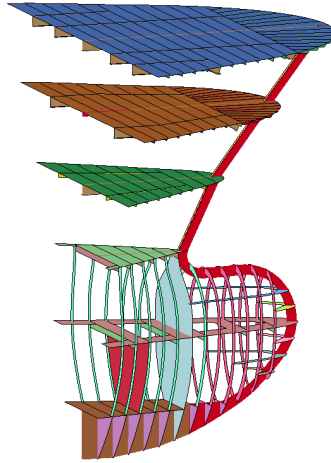


Figure 5.4: Main elements contributing to stiffening of the ship bow section.

When it comes to the load levels for the two parts of the ship section, it is clear that the bulb obtains a more significant force level than the forecastle when being deformed. This can also be explained to some extent by looking at figure 5.4. As can be seen, the bulb has a solid build and many elements contributing to the stiffness. Also, the plate thickness of the bulb (not shown in the figure) is thicker than the forecastle plates. These factors lead to a higher stiffness and thus higher obtained force during deformation.

The original force-deformation curves are rather noisy, as seen by the blue curves in figure 5.3. A part-wise linear approximation has been performed to simplify the curve input in the model file used in the global analyses in USFOS. It is made sure that the linear approximated curves obtain the same collision energy as the original curves, by integrating and comparing the values for each curve.

The integral of the original curves for the forecastle and bulb results in energies of 44.2MJ and 51.2MJ, respectively. The corresponding values for the linear approximations are respectively 44.6MJ and 51.6MJ, which is considered as adequate. Further on, these approximated curves are used in the spring model for the analyses in USFOS.

Chapter 6

Global Analyses of Ship Impacts and Earthquake Loads in USFOS

This chapter includes the results and discussion of the global analysis of different ship impact scenarios and an earthquake event on the OWT. As the chapter contains many figures and curves, the results are presented and discussed for each figure or curve consecutively instead of dividing the two parts.

The results found of interest are presented, and a comparison between the responses of the parked and operational condition is made. The transition piece and monopile structure was found to be little affected by the collision loads. Therefore, it is mainly focused on the response of the tower, RNA and blades. A short assessment of soil utilization is also presented. For the earthquake event, the loads are applied to the OWT in parked condition. This is because the inertia effects of the rotating blades have little influence compared to the large earthquake loads.

The analysis procedure of this work has been to first investigate the response of the global analysis of the beam model of the OWT, before further investigation of local effects, which in this case is buckling of the tower. The global analyses of the beam model obtain essential results of the general behavior and response of the main elements of the OWT. This includes the impact energy, tower top acceleration, and the forces, deformations and plastic utilization of the structural elements, to mention a few.

Even though the local effects are not captured in the beam model, the forces and plastic utilization in the members have been of importance for further refinement of the model. The parts that are found to be critical with respect to material utilization have further been refined and modeled by shell elements, as described in section 4.2.9. By doing this, the local effects are captured. The results of the local buckling analyses are presented in chapter 7.

6.1 Impact energy and force-deformation curves

Common for the collision analyses regarding the parked and operational conditions are the collision energy and the force-deformation curves. To validate that the impact is modeled correctly concerning the input values given for the analysis, the results from USFOS is examined.

First and foremost, the design initial impact energies used in this work is 37MJ and 103MJ, corresponding to impact speeds of 3m/s and 5m/s as described earlier. In figure 6.1, the results for the kinetic energy obtained from USFOS can be seen. The impacts are applied after two seconds.

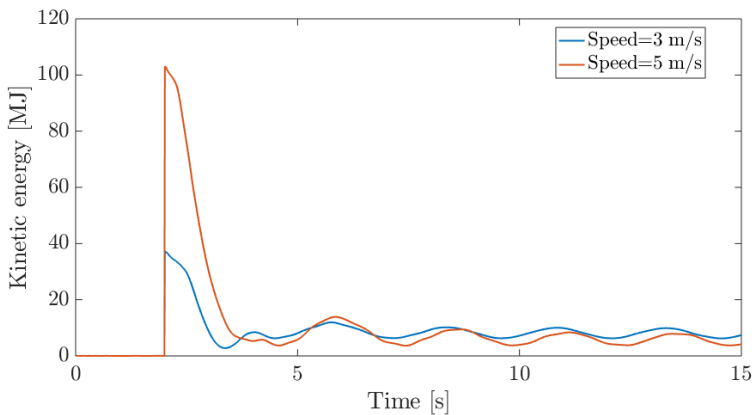


Figure 6.1: Kinetic energy obtained in USFOS for the two impact speeds resulting in collision energies of 37MJ and 103MJ on the OWT.

The results show good correspondence with the initial design energy of 37MJ and 103MJ. The figure shows no kinetic energy for the system until the collision is applied. After the impact, the kinetic energy can be seen to reduce until it oscillates around a value of approximately 10MJ. The decrease in kinetic energy comes from the initial available

collision energy being transformed to strain energy in the bow as it is being crushed. This is obtained by the nonlinear springs representing the forecastle and bow. The remaining part of the kinetic energy comes from the OWT oscillating back and forth after the impact. Especially the RNA and blades connected at the top of the tower contribute to keeping the OWT moving after the impact, as they hold large weight and obtain relatively large velocities.

The force-deformation curves are further examined to verify if the input is correctly implemented in the analyses. A comparison between the input curves described in chapter 5, and the curves from the USFOS analysis for the different impact speeds are presented in figure 6.2 and figure 6.3.

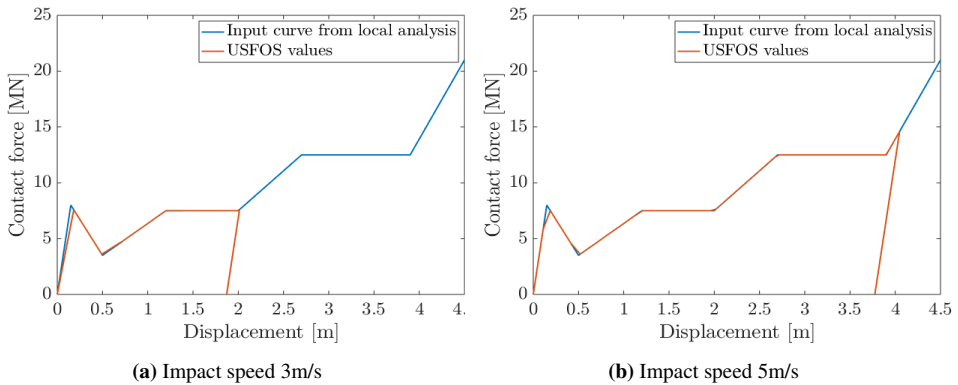


Figure 6.2: Comparison between input force-deformation curves for forecastle and curves obtained from USFOS analyses.

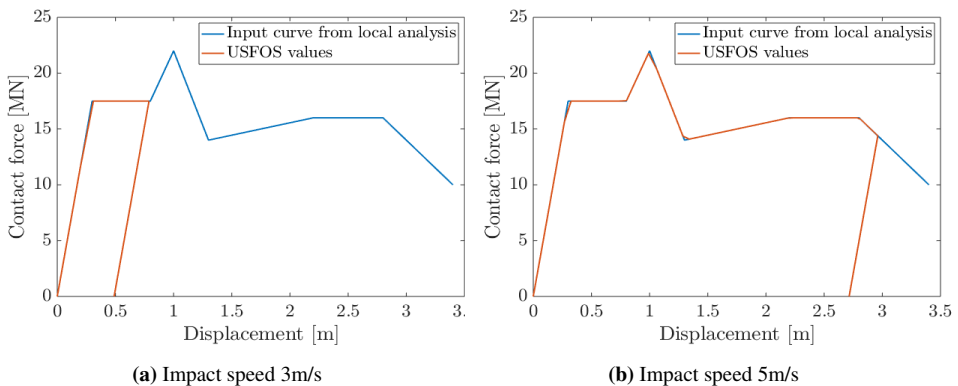


Figure 6.3: Comparison between input force-deformation curves for bulb and curves obtained from USFOS analyses.

The curves show good correspondence, with only small deviations from the input values. Further on, there is one major thing that distinguishes the input curves from the curves obtained from the analyses. The main difference is that the curves from the USFOS analyses show the effect of offloading of the ship, modeled by the linear springs described in section 4.2.7. For the collision event with an impact speed of 3m/s, it can be seen from the figures that the forecastle experiences a deformation of about 2 meters. In comparison, the bulb undergoes approximately 0.8 meters of deformation before offloading. For the event with 5m/s impact speed, the ship experiences a more considerable damage. The forecastle, in this case, has a deformation of 4.1 meters, and the bulb 2.9 meters.

The force-deformation curves can be used to perform simple calculations on the vessel's amount of dissipated energy after crushing. This is done by calculating the area under the USFOS curves (orange in the figure) by integration. For the 3m/s collision speed, the forecastle and bulb obtains energies of respectively 11.9MJ and 8.5MJ, corresponding to a total energy of 20.4MJ. For the 5m/s event, the values are 34.4MJ and 44.5MJ for the forecastle and bow, giving a total of 78.9MJ. The remaining part of the collision energy must be dissipated by the OWT or remain as kinetic energy. These results correspond well with the results discussed regarding the kinetic energy above.

6.2 Analysis of ship collision with parked OWT

In this section, the responses of the parked OWT to the ship impact scenarios are presented. The results of interest include the tower top acceleration, the moment force at the bottom of the tower, and the soil utilization. The results for the two different collision scenarios are presented in the same figures to compare the response amplitudes. In addition, it is convenient to see if the response behavior is different for the two impact energies.

6.2.1 Tower top acceleration

An illustration of the tower top acceleration can be seen in figure 6.4. The impacts are applied after 2 seconds.

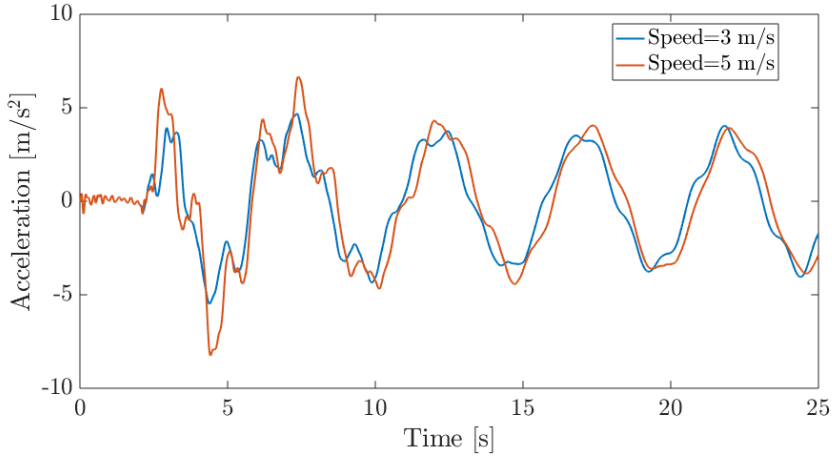


Figure 6.4: Acceleration of the tower top for the two ship impact scenarios with the parked OWT.

Figure 6.4 shows that the response behavior follows approximately the same pattern for the two scenarios, but the response amplitude is as expected larger for the highest impact speed. The oscillating response shows how the tower top moves back and forth after the impact, with the largest peaks obtained during the first oscillating period.

The lowest impact speed achieves a maximum tower top acceleration of 5.5m/s^2 , while the largest impact speed results in an acceleration of 8.3m/s^2 . This corresponds to respectively $0.56g$ and $0.85g$, with g being the gravitational acceleration.

It is hard to obtain literature or manufacturing information regarding the critical accelerations for the tower top of OWTs of the size regarded in this work. However, according to Rasekhi Nejad et al. (2017), who studied a floating 5MW OWT, the common practice in the industry is to have an operational limit of the maximum axial acceleration of the tower top in the range of $0.2\text{-}0.3g$. Compared to the results described for the collision events, the values obtained are over 2 and 3 times larger than the normal practice. This could be critical concerning the operational or structural integrity of the RNA.

6.2.2 Moment force in bottom of tower

The moment force obtained at the bottom part of the tower after the ship impacts, can be seen in figure 6.5.

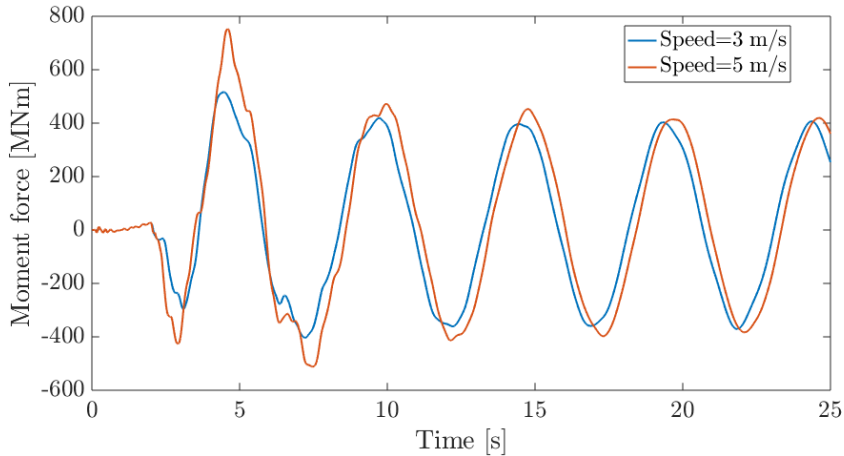


Figure 6.5: Moment force in the bottom part of the tower for the two ship impact scenarios with the parked OWT.

Similar to the tower top response, the response with respect to the moment force in the bottom part of the tower follows the same pattern for both collision speeds. The largest obtained moment force is approximately 520MNm and 750MNm for the 3m/s and 5m/s impact speed, respectively. It is of interest to further examine at which point the largest forces occur. As mentioned earlier, the critical collapse mechanism is for the tower falling towards the colliding ship. Thus, if the most significant force occurs at the point where the OWT is moving towards the ship in the oscillating period, this may lead to the critical collapse.

As both impact scenarios follow the same oscillating response pattern, the highest energy impact is used to illustrate the evolution of response for the bottom part of the tower. The first oscillating period containing the largest moment force values at 2.9, 4.5, and 7.5 seconds is shown in figure 6.6.

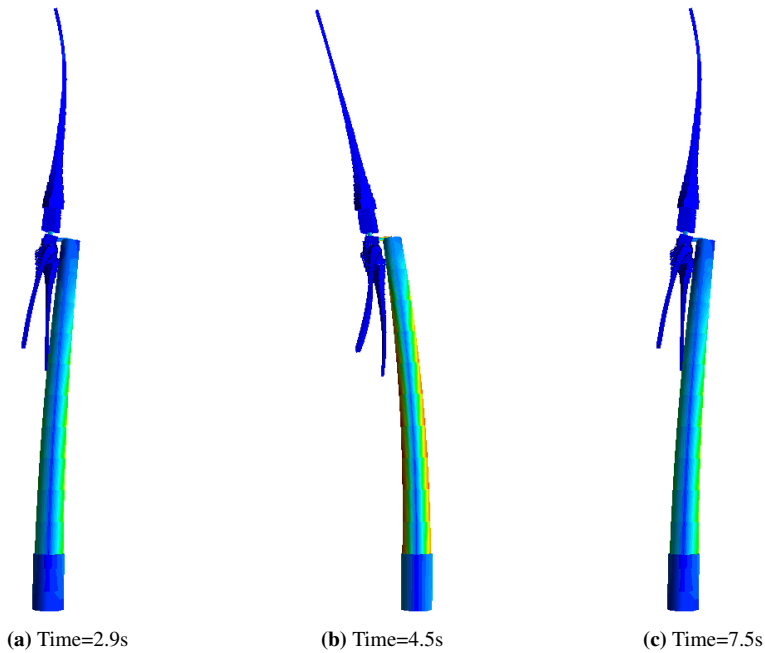


Figure 6.6: Snapshots showing the displacement of the OWT tower at the points obtaining the largest moment force values at the bottom part of the tower. Up-scaled deformations for visual purposes.

Comparing the deformations in figure 6.6 with the corresponding moment force values in figure 6.5, it can be seen that the maximum force occurs after 4.5 seconds which corresponds to the deformation away from the colliding vessel. This is the most desired response as a potential collapse at this moment will lead to the OWT falling away from the vessel.

It is also important to keep in mind that the undesired deformations at 2.9s and 7.5s experience large moment values of 430MNm and 510MNm, respectively. During the response, the tower experience plastic deformation, which can be seen in figure 6.7. The tower may be able to resist the high moment force at 4.5s, but as the material is utilized to a large extent, it could lead to a collapse when the tower moves to the deformed condition at 7.5s. This potential collapse mechanism would lead to the tower falling towards the vessel, which is highly undesirable. The fall direction after collapse will be further investigated in chapter 7.

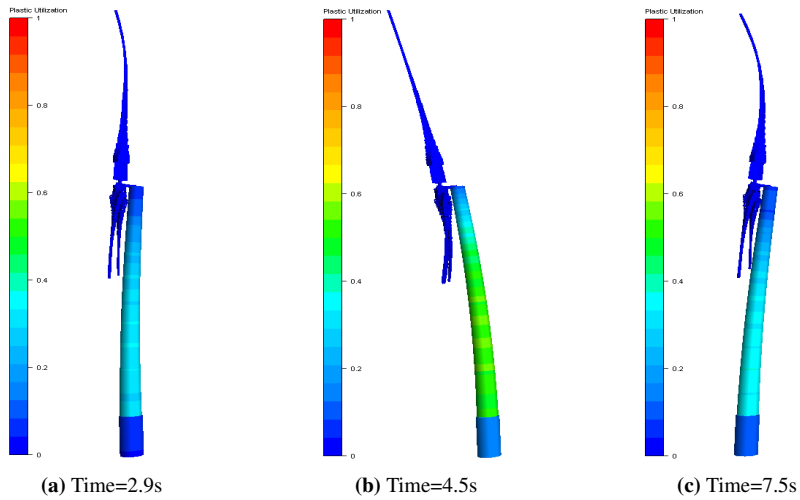


Figure 6.7: Snapshots showing the plastic utilization factors of the OWT tower at the points obtaining the largest moment force values at the bottom part of the tower. Up-scaled deformations for visual purposes. The fringe ranges from 0 (dark blue) to 1 (red).

6.2.3 Soil utilization

The soil-monopile interaction is modeled by 16 auxiliary piles, as described in chapter 4. Figure 6.8 shows the axial force vs. the soil capacity for the auxiliary pile in the upwind condition with the highest utilization. The axial force corresponds to the shear direction of the monopile. The two other directions are found to have low utilization.

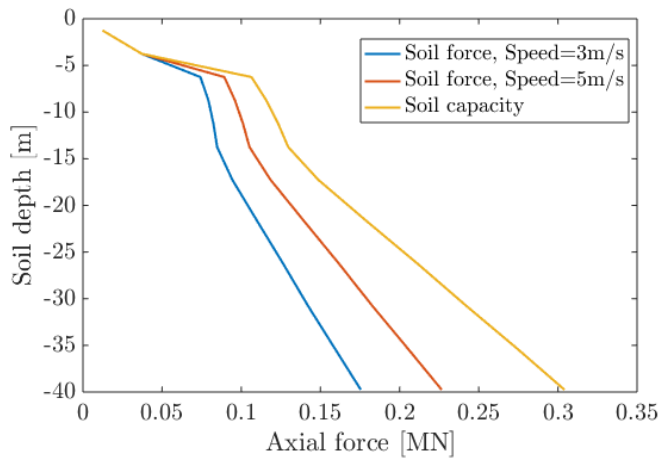


Figure 6.8: Soil utilization comparison between the two ship impact scenarios for the parked OWT.

It can be seen that both collision scenarios have a high utilization of the soil in the upper layer. This is expected as the top 5 meters consist of sand. The soil capacity increases with the increasing depth. This corresponds well with the applied soil model as the lower layers consist of stiff clay that increases in stiffness with increasing depth. Both impacts obtain forces that have a good margin to the soil capacity in the lower soil layers.

An illustration of the point of largest soil utilization corresponding to the results in figure 6.8, can be seen in figure 6.9.

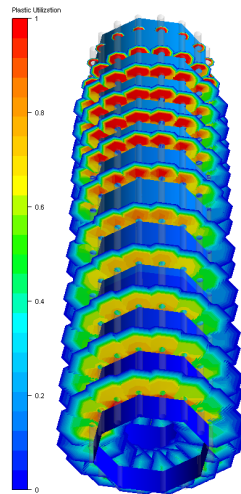


Figure 6.9: Highest soil utilization for largest ship collision event on the parked OWT.

6.3 Analysis of ship collision with OWT in operating condition

The responses investigated for the OWT in the operating condition are similar to the responses of the parked condition. In the same way, the responses from the two different impact speeds are presented in the same figures, in order to compare the response behavior and amplitudes. Also, it is of interest to examine the global response of the blades after the collision to see if the tower clearance is obtained.

6.3.1 Tower top acceleration

An illustration of the tower top acceleration for the OWT in operating condition when subjected to the ship impacts, can be seen in figure 6.10.

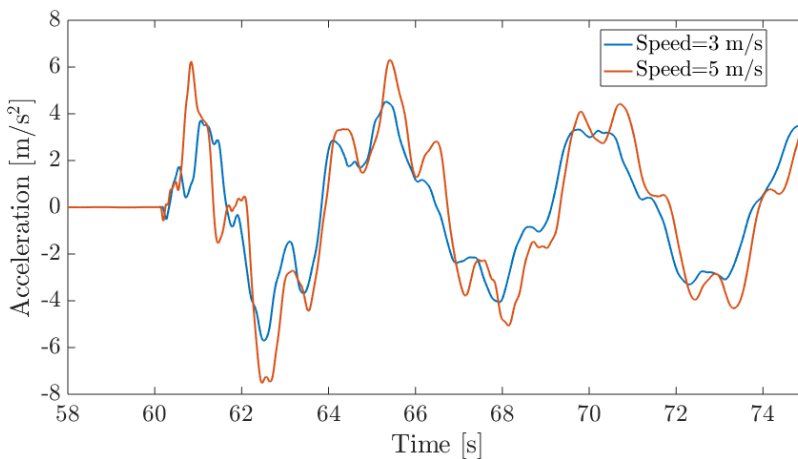


Figure 6.10: Acceleration of the tower top for the two ship impact scenarios with the OWT in operating condition.

The response and amplitudes are similar to the results from the parked OWT. The response for both impact energies follows the same oscillating behavior, with the largest impact energy obtaining larger acceleration amplitudes. The maximum values obtained are 5.7 and 7.5 m/s², corresponding to 0.58g and 0.76g.

6.3.2 Clearance between blade tip and tower

In the case of the operating OWT, it is of interest to investigate the effect on the global response of the blades when subjected to an impact. The blades are highly flexible and can experience large deformations. This may cause contact with the tower and further failure of structural components such as the blades or the RNA. The relative displacement in the global horizontal direction (y-direction) between the tower and blade tip is illustrated in figure 6.11. To account for the model simplifications of neglecting the tilt and cone angles of the blades, as described in section 4.2.2, the extra clearance distance is added in the post-processing of the results.

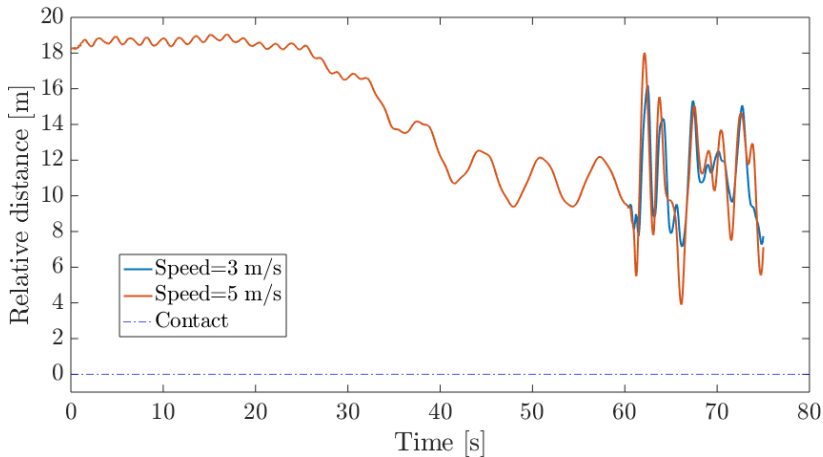


Figure 6.11: Relative horizontal distance between blade tip and tower for OWT in operation, before and after the impacts. Impacts are applied after 60s. Extra tower clearance is added to account for the neglected cone and tilt angle in the model.

As can be seen in figure 6.11, the relative displacement between the tower and blade tip is initially 18.26m, which corresponds to the original tower clearance of the RWT. From approximately 20 to 40 seconds, it can be seen that the relative distance decreases to about 10m. This comes from the application of the wind loads in the same time window. After 40 seconds, it oscillates around this value due to the rotation, until the impact is applied at 60 seconds. A closer view of the response after impact can be seen in figure 6.12.

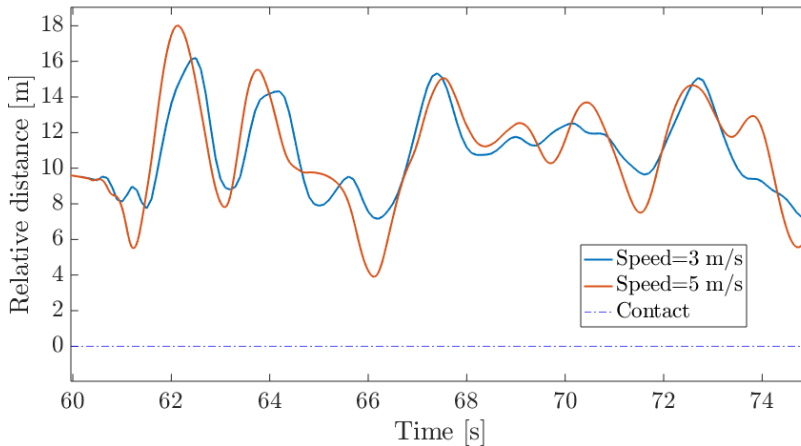


Figure 6.12: Close-up of relative horizontal distance between tower and blade tip for OWT in operation, subjected to the ship impacts. The blue dotted line defines the contact point between the blade tip and tower.

The blue dotted line in figure 6.12 shows the point of potential contact between the blade tip and tower. The figure shows that the blades do not come in contact with the tower. The smallest tower clearance calculated are respectively 7.1m and 3.9m for the lower and larger collision energies. However, it must be mentioned that the blades undergo substantial deformations in short amounts of time, which may cause damage. For the lowest collision speed, the blades undergo a maximum deflection of 8.5m while the larger collision event experiences 12.5m maximum deformation. Both maximum deformations happen in approximately 1 second.

The blade model has the correct flexibility concerning global motion but does not consider local effects such as yielding because the yield strength applied is very large, as described in section 4.2.2. It is thus difficult to assess the potential damage of the blades further with the blade model at hand.

6.3.3 Moment force in bottom of tower

The moment force in the bottom part of the tower for the OWT in operating condition subjected to the ship impacts, is illustrated in figure 6.13.

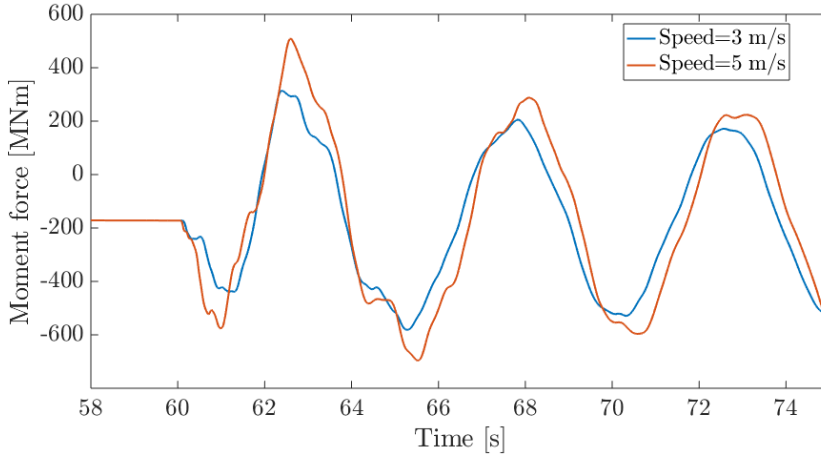


Figure 6.13: Moment force in the bottom part of the tower for the two ship impact scenarios with the OWT in operating condition.

Again, the results are similar to the parked condition. The response for the two impacts follow the same oscillatory behavior pattern, and the largest amplitudes are obtained by the highest energy scenario. However, there is one major part difference that stands out for the OWT in the operating condition when it comes to the moment force in the bottom part of the tower. As can be seen in figure 6.13, the tower has an initial moment force of 172MNm in the bottom part. This comes from the application of the wind- and rotational loads. The inclusion of these loads leads to a downward shift of the moment force curve. This results in an interesting effect on the point of time where the critical force occurs. This will be further described when comparing the parked and operating condition results in section 6.4.

6.3.4 Soil utilization

An equivalent curve for the soil utilization, as presented for the parked OWT, is presented in figure 6.14 for the OWT in operating condition. The two conditions show a similar response of high utilization of the upper layer, and a increasing margin to the soil capacity with increasing depth.

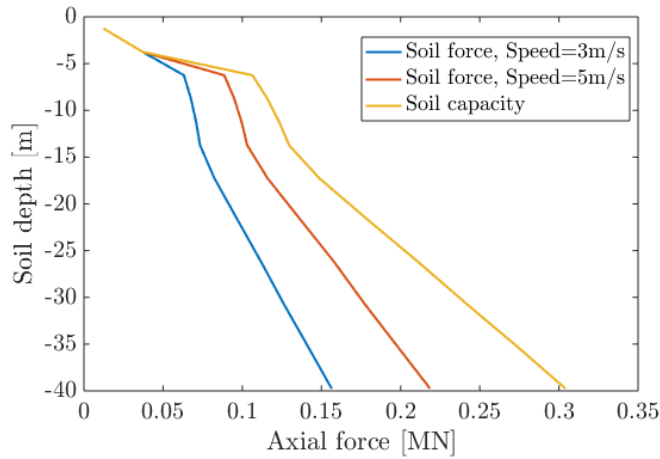


Figure 6.14: Soil utilization comparison between the two ship impact scenarios for the operating OWT.

An illustration of the point of largest soil utilization corresponding to the results in figure 6.14, can be seen in figure 6.15.

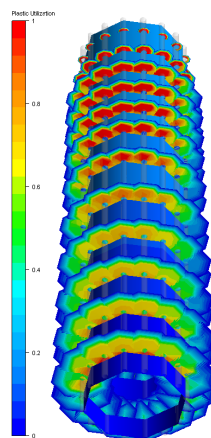


Figure 6.15: Maximum soil utilization during largest ship collision event on the OWT in operation.

6.4 Comparison of impact response between parked and operating condition

Section 6.2 and 6.3 mainly compared the response patterns and amplitudes between the two different collision energies in this work, for the parked and operating condition of the OWT. This chapter uses the same results, but now the comparison is made for the same collision energies but between the two OWT conditions. This is to investigate if the inertia effects of the blades and wind energy influence the response and, if so, the influence is negative or positive with respect to potential failures. The curves for the operating condition are adjusted such that the results can be plotted in the same figures as for the parked condition. The collision is applied after 2 seconds in the comparison plots.

6.4.1 Tower top acceleration

The comparison between the tower top accelerations of the parked and operating conditions of the OWT can be seen in figures 6.16 and 6.17.

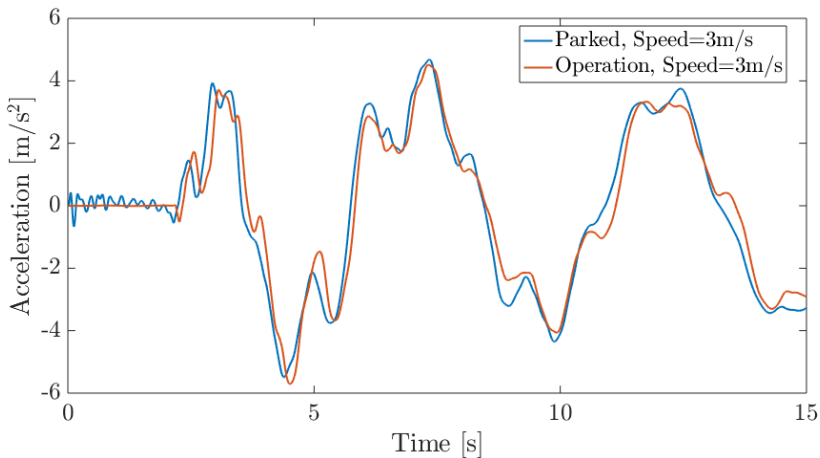


Figure 6.16: Comparison between parked and operating OWT tower top acceleration when subjected to 3m/s ship collision event.

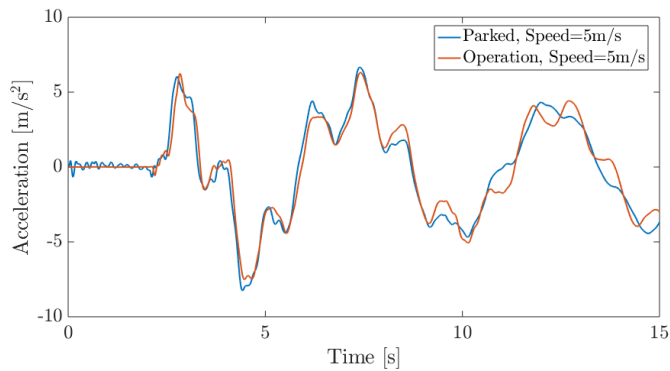


Figure 6.17: Comparison between parked and operating OWT tower top acceleration when subjected to 5m/s ship collision event.

It was initially expected before the analyses that the wind loads would somewhat add to the tower top acceleration acting in the same direction, and decrease it in the opposite direction. However, the results from figure 6.16 and 6.17 show that this is not the case. The curves show little deviation, and the response amplitudes are approximately the same. This indicates that the effect of the impact forces on the OWT is so considerable that the wind loads are insignificant.

6.4.2 Moment force in bottom of tower

The comparison between the bottom tower moment forces of the two conditions of the OWT, can be seen in figures 6.16 and 6.17.

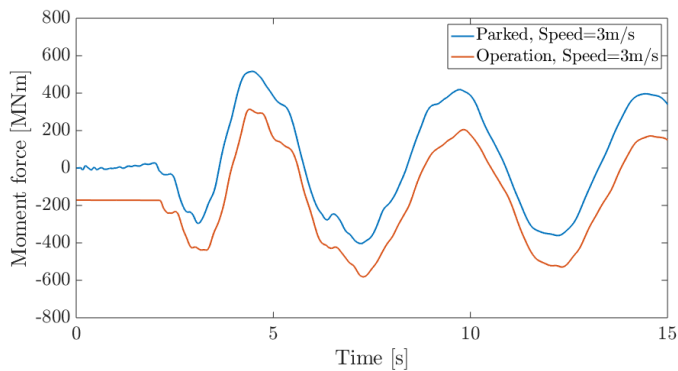


Figure 6.18: Comparison between parked and operating OWT tower top acceleration when subjected to 3m/s ship collision event.

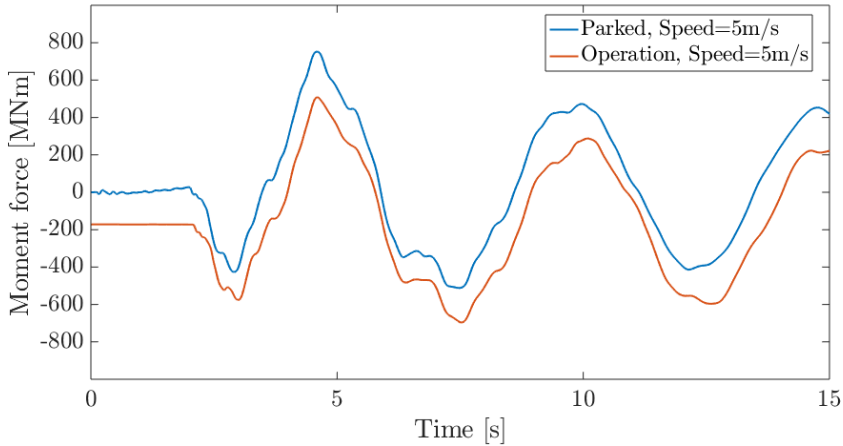


Figure 6.19: Comparison of moment force in bottom part of tower between parked and operating OWT, subjected to 5m/s ship collision event.

These figures show the most interesting response of the global analyses concerning the potential failure mechanisms. As described earlier, the wind loads introduce an initial moment force in the tower before the impact is applied. This leads to a downward shift in the curves for the operating condition. The result of this is that the most significant moment force in the tower for the operating OWT occurs at a later point than for the same collision event with the parked OWT. For both collision events, the parked OWT experiences the most significant force after 4.5s (2.5s after impact), while the operating OWT experiences it after 7.5s (5.5s after impact). By looking at the deformation behavior of the tower in figure 6.6, it can be seen that the maximum force occurs when the OWT is moving towards the ship. This is unlike the parked condition, which has the opposite results. This is not a desirable event if the force is large enough to cause the tower's failure. Thus, the effect of the wind- and rotational loads affects the potential collapse mechanism in this collision scenario, and could in the worst case, cause the turbine to collapse towards the ship.

6.4.3 Soil utilization

A comparison of the soil utilization between the parked and operating OWT subjected to the impacts can be seen in figure 6.20.

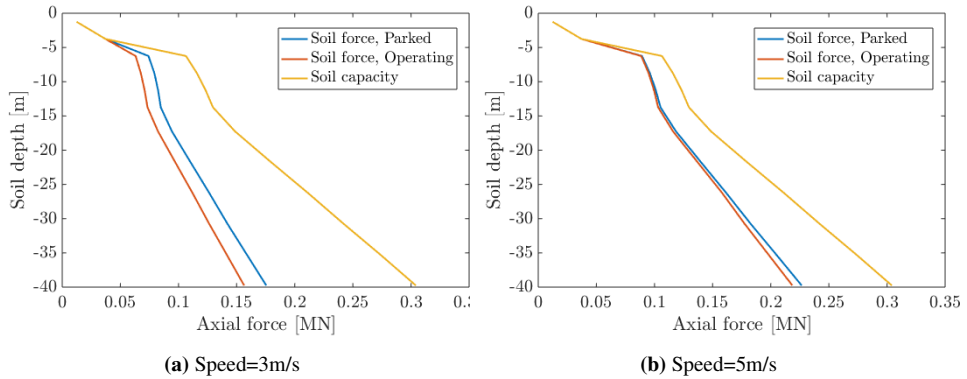


Figure 6.20: Effect of operating condition on the soil utilization for the two collision scenarios.

The figure shows that the loads from the operating condition reduces the soil utilization to some extent as they are applied in the opposite direction of the ship impact load. The effect is larger for the impact speed of 3m/s. For the largest impact, the curves are quite similar.

6.5 Analysis of earthquake loads on OWT

An investigation of the OWT response to an earthquake has been performed. The analyses have been conducted for both parked and operating conditions for the OWT in the global x- and y-direction separately. The global x- and y-direction corresponds to the blade direction and wind direction, respectively. The applied earthquake displacement history has also been up-scaled to see the effect of a potentially larger earthquake and to trigger a buckling failure of the OWT. This will be further described in chapter 7.

After examining the results, it is found that the earthquake in the y-direction causes the most significant and critical responses. Thus, the results from this loading direction are presented here. In addition, the operational condition's effects were found to have little influence on the response, as the earthquake is the dominating force. Due to this, there is no comparison between the parked and operational condition, but rather a presentation of the results found of interest for single load cases and operational conditions. This includes

the same responses investigated for the collision events to compare the response magnitudes between the accidental events. It also consists of an investigation of the correlation between the modal shapes and modal frequencies of the structure, with the frequency components in the earthquake displacement history.

6.5.1 Tower top acceleration

The tower top acceleration for the parked OWT during the earthquake is illustrated in figure 6.21.

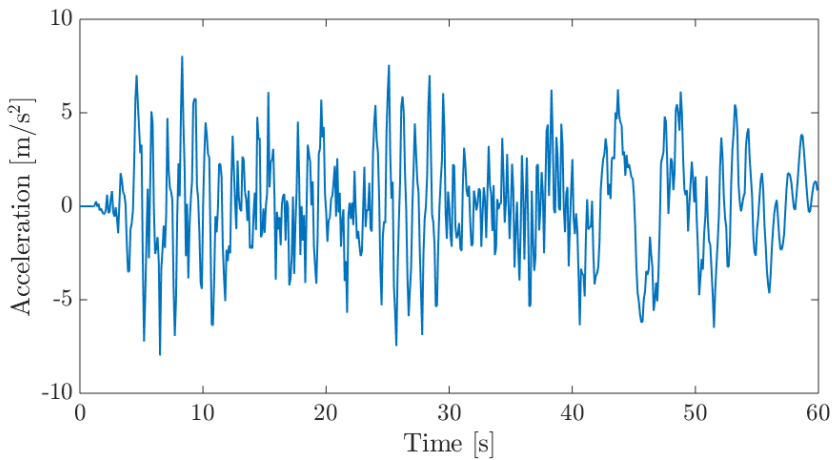


Figure 6.21: Time history of tower top acceleration in global y-direction during earthquake on OWT in parked condition.

The OWT experiences large accelerations in both positive and negative horizontal direction throughout the loading history. The maximum obtained acceleration is approximately 8.0m/s^2 , or $0.82g$, which is slightly lower than the maximum of $0.85g$ obtained for the largest collision event described earlier. It is thus also way above the operational limit of $0.2\text{-}0.3g$ explained earlier. Even though the maximum acceleration is slightly lower, the accelerations are highly fluctuating for the earthquake compared to the more steady oscillating response for the collision event, which is expected.

6.5.2 Clearance between blade tip and tower

The tower clearance of the blades was found to have a margin of 7.1m and 3.9m for the collision scenarios with the OWT in operating condition. For comparative reasons, it has been of interest to see if the earthquake causes contact between the tower and blades in the operating condition. Figure 6.22 shows the relative distance between the tower and the blades. The earthquake is applied after 60 seconds when the blades are at the maximum rotational speed.

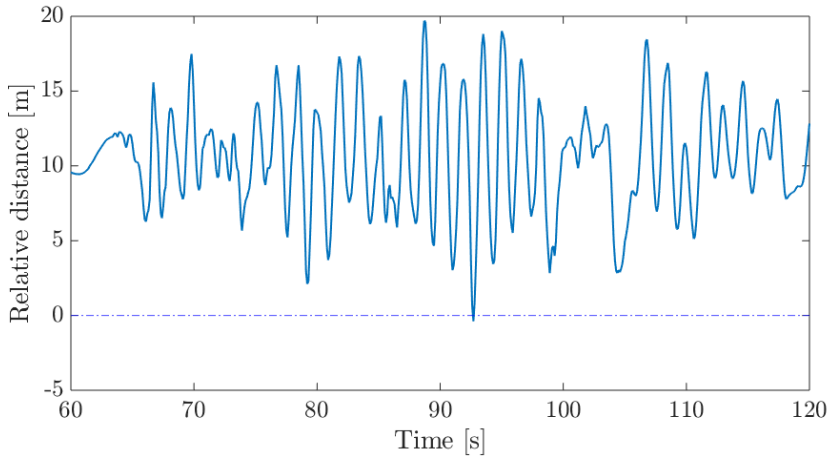


Figure 6.22: Relative horizontal distance between tower and blade tip for OWT in operation, subjected to earthquake. The blue dotted line defines the contact point between the blade tip and tower.

Similar to the collision events, the blades experience substantial deformations in short periods. Also, unlike the collision scenarios, the earthquake causes the blades to hit the tower while in operation, which can be seen at the crossing point of the blue dotted line in figure 6.22. The contact force is not modeled in this work, but could be substantial and potentially cause large damage to the blades and the RNA.

6.5.3 Moment force in bottom section of tower

The moment force in the bottom part of the tower for the parked OWT during the earthquake is illustrated in figure 6.23.

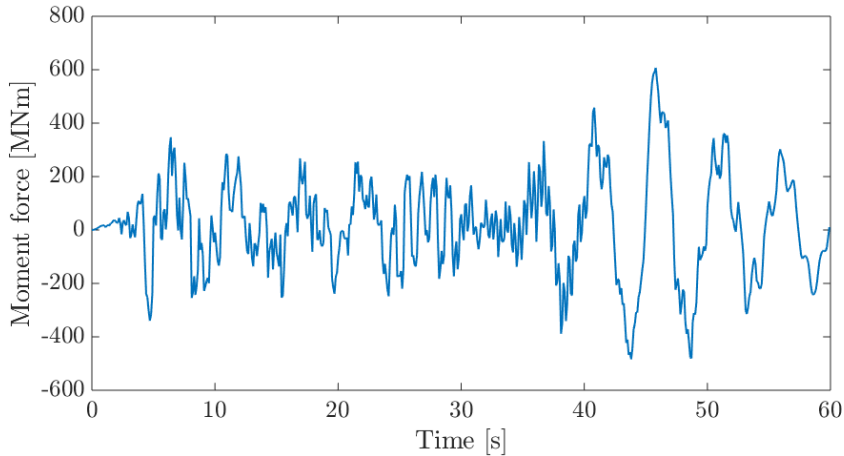


Figure 6.23: Time history of moment force in bottom part of tower during earthquake on OWT in parked condition.

Following the same nature as the acceleration response, the moment force in the bottom part of the tower also experiences a highly fluctuating response. It can be seen that the moment force varies between approximately 300MNm in both oscillating directions during the first 40 seconds of the time history. After about 45s the moment force obtains the maximum value of 607MNm. Compared to the collision events, this value lies in between the two impacts, which resulted in 520MNm and 750MNm in the tower.

The most significant moment force can be explained by looking at the soil displacement history in figure 4.15. The soil has the largest displacement in one direction of about 1 meter around the same time as the most significant moment force occurs. This significant movement results in a considerable tower top acceleration, which again causes the large moment force in the tower. This large response is also possible to observe in the acceleration history in figure 6.21. Unlike the highly oscillatory behavior until approximately 40 seconds, it can be seen that there is a "gap" in the plot. This gap shows that the tower top experiences a significant one-directional motion instead of oscillating back and forth.

6.5.4 Comparison between the structural response and the mode shapes and natural frequencies of the OWT

After a visual inspection of the OWT when subjected to the earthquake, the structural response showed some interesting results. The deformation patterns of the blades and tower showed resemblance to some of the mode shapes that were found by the eigenvalue analyses. Due to this, it was decided to investigate if there were any dominating frequency components in the displacement history of the earthquake, that could cause any dynamic amplification of the mode shapes in the response.

The frequency components of the soil displacement history is obtained by performing a Fourier transform of the time domain data, resulting in the displacement history being transferred to the frequency domain. Further on, the displacement amplitudes are normalized. The time-domain and corresponding frequency domain of the displacement history are shown in figure 6.24 and 6.25 respectively.

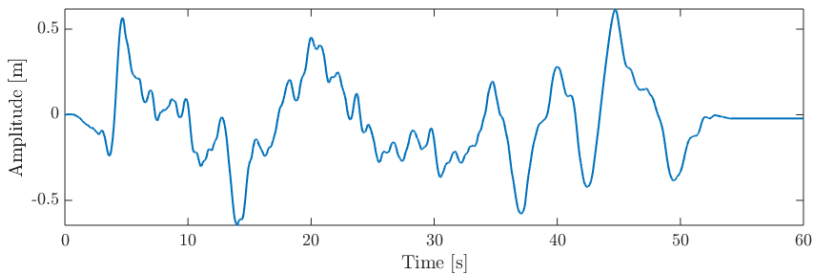


Figure 6.24: Time domain of the soil displacement history of the earthquake.

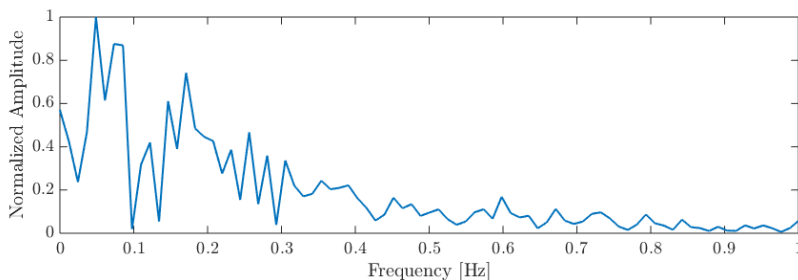


Figure 6.25: Frequency domain of the soil displacement history of the earthquake. Displacement amplitudes are normalized on the y-axis.

Figure 6.25 shows that the soil displacement history contains a broad range of frequency components. It also indicates that the soil displacement amplitudes are dominated by the lower frequencies, with the most significant values being in the frequency range of 0.05-0.2Hz. These frequencies correspond to periods of 5-20 seconds. These results only show the frequency components for the earthquake itself. The structural interaction and dynamic amplification effects must be taken into account to investigate the connection with the OWT response.

The relative displacement between a point on the pile and two other points are examined to investigate the effect of the pile displacement on the OWT response. The two points are the tower top and the blade tip of the parked OWT. A Fourier transform is performed on the time domains of these relative displacements to obtain the dominating response frequencies of the OWT. The results can be seen in figure 6.26 and 6.27.

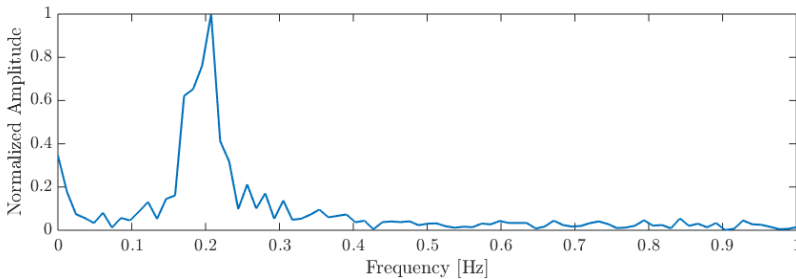


Figure 6.26: Frequency domain of the relative displacement history between the pile and the tower top of the parked OWT subjected to the earthquake. Displacement amplitudes are normalized on the y-axis.

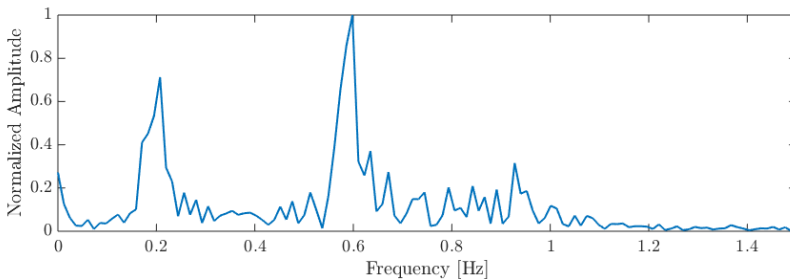


Figure 6.27: Frequency domain of the relative displacement history between the pile and the blade tip of the parked OWT subjected to the earthquake. Displacement amplitudes are normalized on the y-axis.

It can be seen from the frequency domain plots that some frequencies dominate the largest response amplitudes. These are approximately 0.2Hz in figure 6.26 and at 0.2Hz and 0.6Hz in figure 6.27. These will be compared to the natural frequencies and modes obtained by the eigenvalue analysis for the full system.

An overview of some of the obtained vibration modes with the corresponding natural frequencies is shown in table 6.1.

Table 6.1: A selection of natural frequencies and corresponding vibration modes obtained from the eigenvalue analysis of the complete OWT model performed in USFOS.

Mode	f_n [Hz]	T_n [s]
1st Tower fore-aft	0.21	4.71
1st Tower side-side	0.21	4.67
1st Blade Asymmetric Flap-wise Yaw	0.53	1.88
1st Blade Asymmetric Flap-wise Tilt	0.57	1.74
1st Blade Collective Flap	0.62	1.61
1st Blade Asymmetric Edgewise 1	0.89	1.12
1st Blade Collective Edgewise	0.90	1.11
1st Blade Asymmetric Edgewise 2	0.90	1.11
2nd Tower fore-aft	1.12	0.89
2nd Tower side-side	1.14	0.88

The earthquake is applied in the global y-direction (wind direction). Therefore, the modes of interest for the response are acting in this direction. These include the fore-aft modes of the tower and the flap-wise modes of the blades. Comparing these modes with the plots in figure 6.26 and 6.27, it can be seen that there are correlations between the maximum responses and some of the modes.

The maximum displacement of the tower top represented in figure 6.26, can be seen to correspond with the frequencies of the 1st tower fore-aft mode with a natural frequency of 0.21Hz. For the blade tip, the maximum displacements correspond well with the 1st tower fore-aft mode, as well as the flap-wise blade modes around 0.6Hz. This is also logical as the tower top response will influence the blades attached at this point. From these results, it is clear that the earthquake loads include frequency components that coincide with some of the structure's natural frequencies. This results in a dynamic amplification of the response

modes corresponding to these frequencies.

Some snapshots are presented in figure 6.28 and 6.29. The figures show the resemblance between the earthquake response and the modal shapes of the OWT. The snapshots are taken at the time of response when the dominant mode shapes are easily observable.

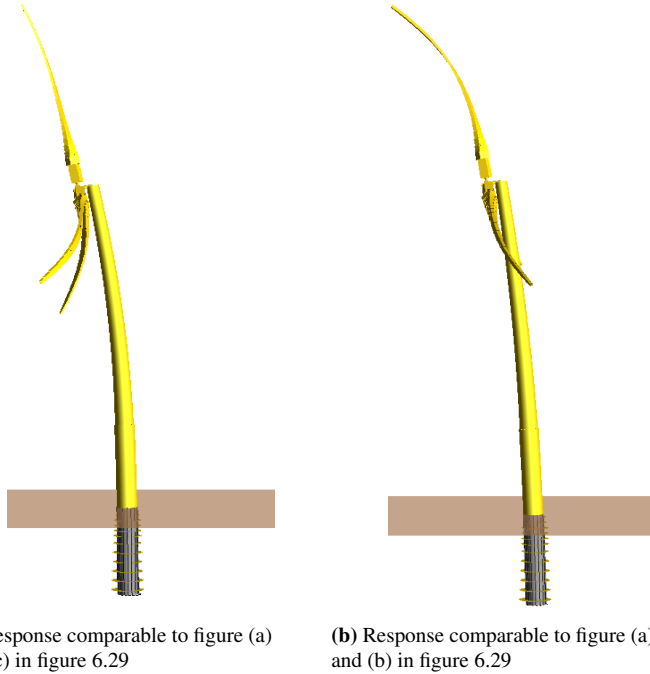


Figure 6.28: Snapshots showing the actual response of the OWT during the earthquake. Up-scaled for visual purposes.

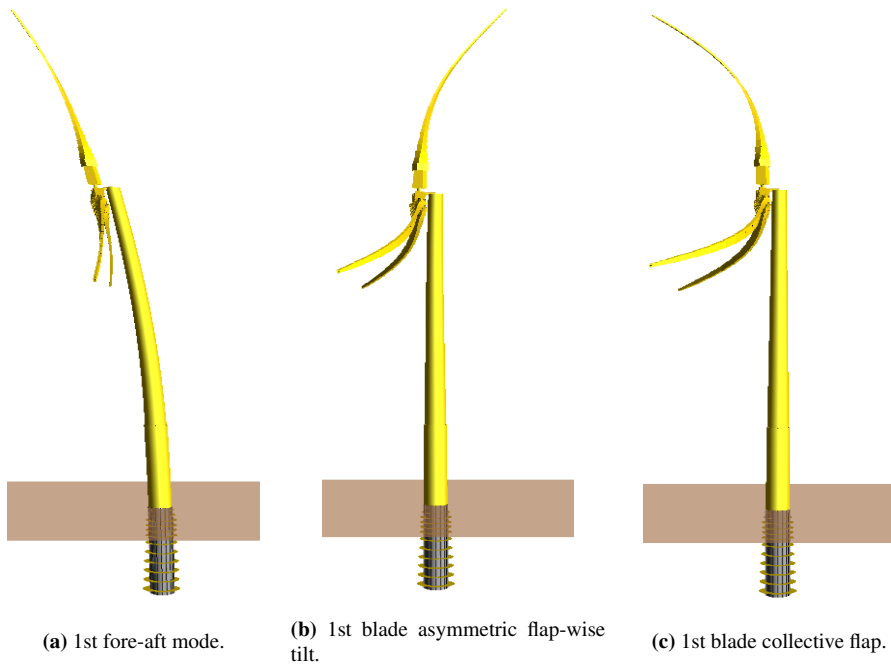


Figure 6.29: Snapshots showing the modal shapes of the OWT. To be compared with the actual response in figure 6.28. Up-scaled for visual purposes.

Local Buckling Analyses of the OWT Tower

After examining the results from the global analyses described in chapter 6, some results were found of interest to investigate further. The interesting results especially concerns buckling of the tower, as the tower was found to have a high utilization for several of the accidental events analyzed. Concerning the ship collision scenarios, the 103MJ collision event on the parked OWT was most critical when considering the lower part of the tower. For the earthquake event, the middle part of the tower was found to experience the most significant stresses. These events will be presented in the following.

7.1 Simple calculations of buckling capacity

Some simple hand calculations are presented to indicate the tower's structural utilization concerning buckling. Simple considerations regarding imperfections and plasticity are taken into account. The potential critical scenarios are then detected by comparing the results from the global analyses with the calculated critical buckling stresses.

The buckling of a cylinder generally occurs due to a combination of loads such as axial compression, bending, external pressure and torsion, to mention a few. This normally requires interaction formulas to calculate the buckling resistance. However, in this work, all the investigated scenarios are dominated by bending. Due to this, it is decided to use

simple formulas for the buckling resistance when subjected only to bending. This does not have a large effect on the final result. The formulas used are obtained from Amdahl (2010).

7.1.1 Bottom part of tower

The main dimensions used in the buckling capacity calculations for the bottom part of the tower are presented in table 7.1.

Table 7.1: Main dimensions of bottom part of tower used in buckling capacity calculations.

Parameter	Value	Unit
Radius, r	4.15	m
Thickness, t	46	mm
Elastic modulus, E	210	GPa
Yield stress, σ_y	355	MPa

The critical elastic stress is found by equation 7.1:

$$\sigma_E = 0.605 \frac{Et}{r} = 1408 \text{MPa} \quad (7.1)$$

As described in chapter 3, the effect of initial imperfections are significant on the buckling capacity of the cylinder. This effect is included by using a so-called "knock-down" factor ρ_k given by equation 7.2.

$$\rho_k = \frac{0.5}{\sqrt{1 + \frac{r/t}{300}}} = 0.438 \quad (7.2)$$

Thus, the elastic buckling stress when taking imperfections into account becomes:

$$\sigma_{E,cr} = \rho_k \cdot \sigma_E = 0.438 \cdot 1408 \text{MPa} = 617 \text{MPa} \quad (7.3)$$

Finally, the effect of plasticity is taken into account by using a reduced slenderness factor $\bar{\lambda}$ found by using equation 7.4, and inserting it into equation 7.5 to obtain the plasticity reduction factor ϕ .

$$\bar{\lambda} = \sqrt{\frac{\sigma_y}{\sigma_{E,cr}}} = 0.758 \quad (7.4)$$

$$\phi = \frac{1}{\sqrt{1 + \bar{\lambda}^4}} = 0.867 \quad (7.5)$$

The critical buckling stress for the bottom part of the tower, including effects from imperfections and plasticity, is then found by equation 7.6:

$$\sigma_{cr} = \phi \cdot \sigma_y = 0.867 \cdot 355\text{MPa} = 308\text{MPa} \quad (7.6)$$

7.1.2 Mid part of tower

An equivalent calculation performed for the bottom section has been done for the mid-section of the tower as well. The main dimensions for this section can be seen in table 7.2.

Table 7.2: Main dimensions of mid part of tower used in buckling capacity calculations.

Parameter	Value	Unit
Radius, r	3.59	m
Thickness, t	36	mm
Elastic modulus, E	210	GPa
Yield stress, σ_y	355	MPa

For the midsection, the critical buckling stress is approximately 298MPa, which is slightly lower than for the bottom section.

7.2 Overview of results from the global analyses

The critical buckling stresses estimated in section 7.1 are further compared to the bending stresses in the two sections that were found in the global analyses. The results presented from the global analyses include the two collision scenarios and two different scales of the earthquake for the parked and operating conditions of the OWT. The bending stress values are the highest obtained value for the respective sections for each loading scenario. By comparing the values from the tables with the critical buckling stresses, you get an indication of which load case that might experience a buckling failure. These critical cases are analyzed by using shell elements to capture the eventual local buckling.

7.2.1 Results from collision analyses

The maximum obtained bending stresses for the collision analyses can be seen in table 7.3 and 7.4.

Table 7.3: Maximal obtained bending stress in bottom section of tower when subjected to ship collision events. Stresses exceeding the buckling stress are marked with bold text.

Collision	Speed=3m/s	Speed=5m/s
Parked	225 MPa	326 MPa
Operating	252 MPa	198 MPa

Table 7.4: Maximal obtained bending stress in mid section of tower when subjected to ship collision events. Stresses exceeding the buckling stress are marked with bold text.

Collision	Speed=3m/s	Speed=5m/s
Parked	265 MPa	355 MPa
Operating	242 MPa	312 MPa

The results show that the collision speed of 3m/s does not result in stresses that exceed the critical buckling stress for any of the two sections. The largest collision speed, however, results in bending stresses that exceed the calculated critical buckling stress. This is the case for the bottom part of the parked OWT, and for both conditions for the midsection of the tower. The results also show that the parked condition obtains the most considerable bending stresses. This corresponds well with the comparison between the parked and operating conditions in chapter 6. The largest collision on the parked OWT is further examined by shell modeling of the bottom and midsections.

7.2.2 Results from earthquake analyses

The maximum obtained bending stresses for the earthquake analyses can be seen in table 7.5 and 7.6. The original earthquake is included, in addition to the same earthquake up-scaled by a factor of 2.

Table 7.5: Maximal obtained bending stress in bottom section of tower when subjected to earthquake events. Stresses exceeding the buckling stress are marked with bold text.

Earthquake	Scale=1	Scale=2
Parked	263 MPa	355 MPa
Operating	296 MPa	355 MPa

Table 7.6: Maximal obtained bending stress in mid section of tower when subjected to earthquake events. Stresses exceeding the buckling stress are marked with bold text.

Earthquake	Scale=1	Scale=2
Parked	280 MPa	355 MPa
Operating	310 MPa	355 MPa

The results show that the bending stresses in the bottom section is close to buckling stress, but does not reach it during the original earthquake loads. The midsection is the most critical concerning buckling as it is close to the parked condition's buckling stress and exceeds it for the operational condition. Due to computational limits, the parked condition is analyzed further by shell elements as it requires significantly less computational capacity than the OWT in operation. This is due to the large amount of time needed to obtain the rotational speed of the blades.

7.3 Comparison between imperfection application methods

As described in chapter 3, the imperfections are introduced by two different functions in USFOS, namely BUCKMODE and GIMPER. These apply the imperfections by eigenvalue considerations and dents, respectively. A comparison of the two methods is made to identify any significant differences in the response.

Concerning the global response, the two methods result in the same response and do not have any significant differences. The dent was also applied in the downwind direction for the operating turbine in an attempt to trigger a collapse mechanism towards the ship. However, this did not happen for the dent applied.

Even though the global responses are similar, the local effects are quite different when examining the response of the shell sections with the two different imperfection methods. Figure 7.1 shows the equivalent strain distribution for each of the methods at the point of maximum moment force in the bottom section after the collision.

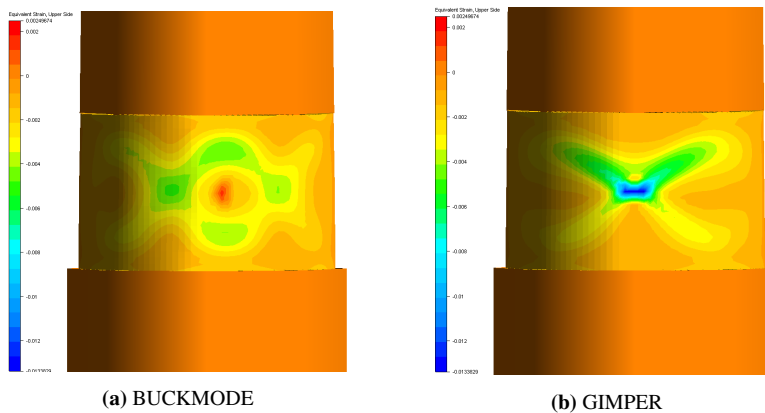


Figure 7.1: Comparison of the strain distribution between the two imperfection application methods used in the buckling analyses in USFOS. Fringe ranges from -0.013 (dark blue) to 0.002 (red).

It is clear that the local effects are different for the two methods. The strains follow the applied imperfections. While the strains are more distributed along the circumference for the BUCKMODE method, which has imperfections around the whole cylinder, the strains for the GIMPER method are more concentrated at the applied dent. This is as expected. The BUCKMODE method was chosen to be used for the rest of the work since the methods showed no difference in the global response.

7.4 Buckling response during ship collision

Both the bottom and midsection were found to be critical for the largest collision on the parked OWT. Figure 7.2 shows the plastic utilization for both sections at the most critical point during the impact.

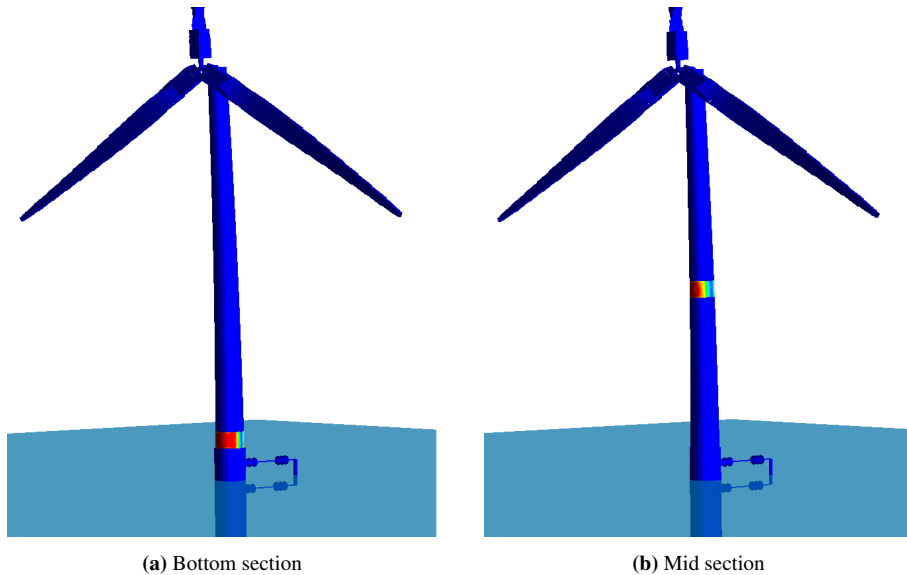


Figure 7.2: Plastic utilization of bottom and mid section at most critical point during the largest ship impact scenario with the parked OWT. Red color represents full plastic utilization.

The figure clearly shows that both sections experience a high plastic utilization on the upwind part of the tower, i.e., on the opposite side of the impact point. This is favorable, as described earlier. However, a total collapse of the structure did not occur during the event. The sections are therefore examined closer. Figure 7.3 shows a close-up of the equivalent strain for the two parts at the same point as above. The fringe range is equal to compare the buckling evolution between the two sections.

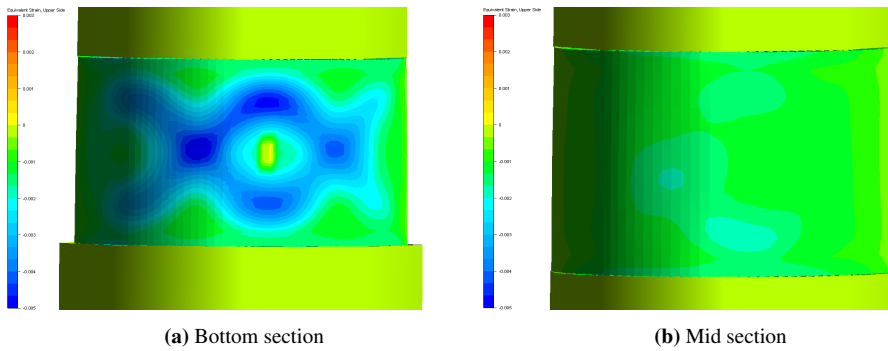


Figure 7.3: Close up of equivalent strain of bottom and mid section at most critical point during the largest ship impact scenario for the parked OWT. Fringe ranges are equal for both cases for comparative purposes. Fringe ranges from -0.005 (dark blue) to 0.003 (red).

After a closer examination, it is found that both sections have initialized a buckling behavior. Figure 7.3 shows that the bottom section has obtained a significantly larger buckling behavior than the midsection at the same point and is expected to be the critical part concerning the collapse. This was not expected when compared to the results in table 7.3 and 7.4, where the midsection was found to have the most considerable bending stresses exceeding the buckling stress.

The thickness is reduced by 10%, to trigger a collapse of the structure. The results can be seen in figure 7.4.

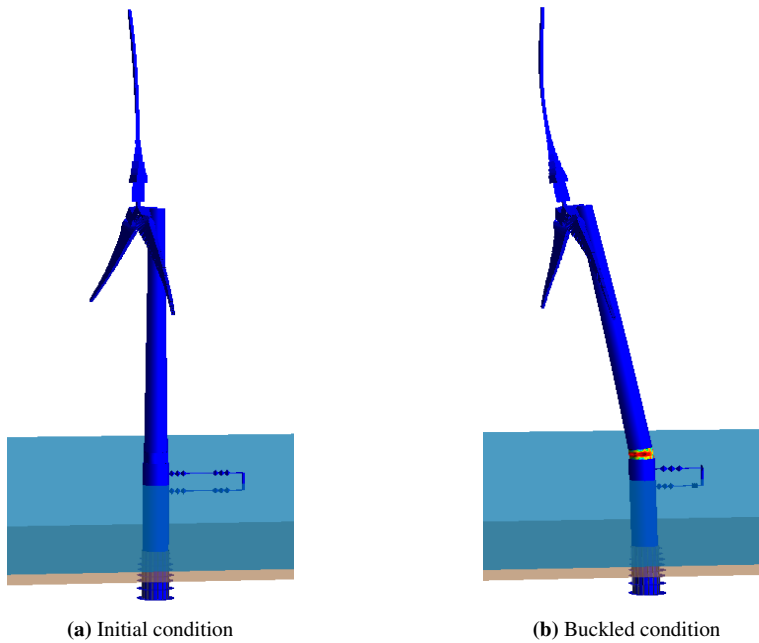


Figure 7.4: Buckling collapse of the OWT as a result of a 10% reduction of the wall thickness of the tower. The deformations are scaled up for visual purposes.

The figure shows that the bottom section buckles and causes the OWT to collapse away from the vessel. A close-up visualization of the collapse mechanism of the bottom section can be seen in figure 7.5.

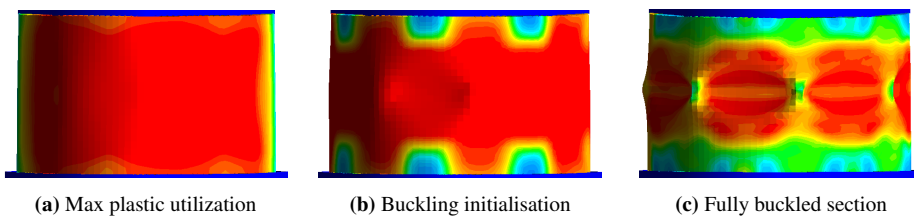


Figure 7.5: Snapshots showing the evolution of the buckling of the bottom part of the OWT tower. The colors represents the plastic utilization factor, and ranges from 0 (dark blue) to 1 (red).

7.5 Buckling response during earthquake

Similar to the collision scenario described above, the OWT does not collapse during the earthquake, but the midsection does experience a high plastic utilization and buckling behavior. This can be seen in figure 7.6.

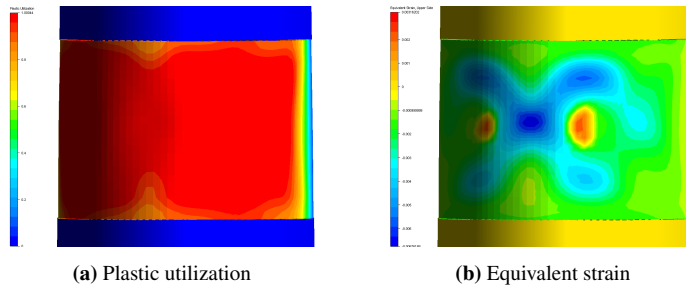


Figure 7.6: Close-up of plastic utilization and equivalent strain of mid section at most critical point during the earthquake on the parked OWT. Fringe ranges from 0 (dark blue) to 1 (red) for the plastic utilization factor and from -0.007 to 0.003m for the equivalent strain.

The earthquake is scaled up by a factor of 2, to trigger a buckling of the midsection of the tower. The results can be seen in figure 7.7.

As can be seen, the OWT collapses downwind. For the earthquake event, the collapse has no favorable direction. The evolution of collapse is similar to the case of the bottom section. This can be seen in figure 7.8.

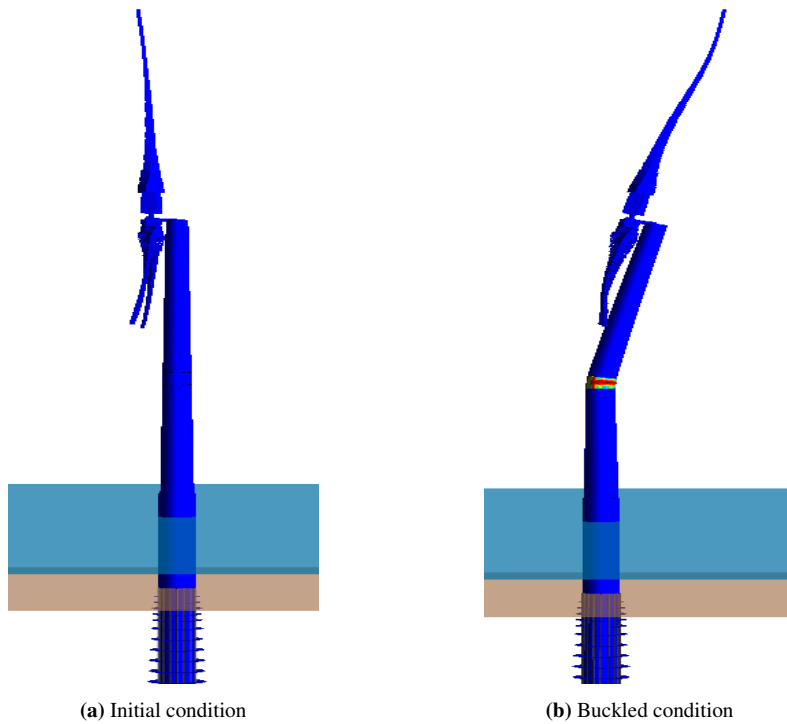


Figure 7.7: Buckling collapse of the OWT as a result of the earthquake scaled up by a factor of 2. The deformations are scaled up for visual purposes.

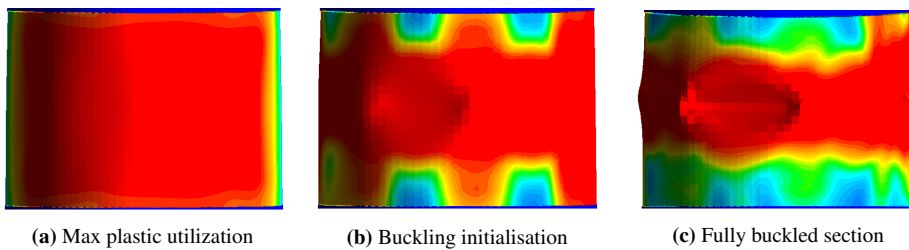


Figure 7.8: Snapshots showing the evolution of the buckling of the mid part of the OWT tower. The colors represent the plastic utilization factor, and range from 0 (dark blue) to 1 (red).

Conclusions and Recommendations for Further Work

The main goal of this thesis has been to investigate in more detail the response of a monopile supported offshore wind turbine, subjected to ship impacts. In addition, an assessment of the OWT response during an earthquake event has been performed. This chapter summarizes the work that has been done and the main results that has been found. Finally, recommendations for further work are given for potential extensions of this work.

8.1 Conclusions

A finite element model representing a 10MW offshore wind turbine, mounted on a monopile at 30m depth, has been established using the computer program USFOS. The blades can be rotated, making the model representative for both a parked and operational condition. The soil conditions are adapted from the Dogger Bank region in the North Sea. The effect of wind drag- and lift forces have been modeled as nodal loads distributed along the blades in the wind direction.

A local analysis of the ship damage of a 7500 tons displacement with a bulbous bow subjected to an impact with the OWT transition piece has been conducted. The force-deformation curves obtained have been linearized and transferred to the global model to represent the strength and deformation characteristics of the ship. The total energies found to be dissipated as strain energy in the ship were 20.4MJ and 78.9MJ for the two impacts.

Global analyses have been conducted for ship impact speeds of 3m/s and 5m/s, corresponding to initial kinetic energies of 37MJ and 103MJ. The collision analyses include the OWT in both parked and operating conditions. Nonlinear and linear springs are used in the global USFOS analyses to model the bow crushing that was analysed in LS-DYNA, and the offloading of the ship after the impact.

The OWT showed high resistance against collapse for all collision scenarios, especially for the lowest collision energy events. The transition piece and monopile support structure were little affected in general. The soil showed high utilization of the upper layers and lower utilization of the deeper layers. The responses found to be most critical were the tower bending stress and accelerations of the nacelle. The tower experienced a maximum bending stress of respectively 326MPa and 355MPa in the bottom and midsection, when subjected to the largest collision speed. Both exceeded the buckling capacity of the sections that was found to be 298MPa and 308MPa.

The operating condition showed little to no effect on the acceleration of the tower top, but had some effect on the soil utilization and the moment force obtained in the tower. Concerning the soil utilization the effect was positive as the operating condition lowered the soil utilization. The effect was higher for the smallest impact energy. The operating condition had a negative effect concerning the collapse of the tower. It resulted in the maximum force in the tower being obtained when the OWT is moving towards the vessel, which is undesirable.

Analysis of glancing blow impacts with representative global motion properties of the ship has not been done. Instead, global analyses of the OWT subjected to an earthquake event were performed. The OWT showed high resistance against global collapse in this case as well, but obtained high bending stresses in the middle of the tower. These exceeded the buckling capacity stress of 298MPa. The response also turned out to be dominated by the tower fore-aft and blade flapping modes found in the eigenvalue calculations.

The bottom and midsection of the tower has been modelled by shell elements. Local imperfections have been introduced and an investigation of possible local buckling of both sections have been performed for the most critical collision and earthquake events. The sections showed an initialization of buckling behaviour, but did not lead to a total collapse for the original events. To trigger collapse, the thickness was reduced for buckling of the bottom part, and an up-scaled earthquake was used to cause the midsection to buckle. All collapse mechanisms were found to be desirable, as they resulted in the wind turbine falling away from the vessel.

8.2 Recommendations for further work

The following recommendations for further work on this subject are:

- An investigation of the collision events in different directions should be performed to compare with the collision direction used in this case.
- Modeling of a jacket and tripod support structure to compare the response of the most used substructures would be interesting, to see which proves to be most advantageous at different load conditions and water depths.
- As the collision events are highly individual, a parameter study should be performed. Parameters that could be studied are e.g: tower and monopile thickness, wind loads, soil conditions, height of impact point.
- This work considers a standard supply vessel, and it could be of interest to investigate the response when impacted by other vessels. An example is a drifting tanker with considerably larger collision energy than considered in this work.
- The monopile and transition piece model used in this work is simple, and a more detailed modeling of these can be done. The dimensions should also be challenged to investigate potential collapse mechanisms of the support structures.
- The effect of waves are not included here and should be investigated further. This includes the effect of the impact point due to waves for example. The effect of wave loading on the post-collision OWT could also be interesting to examine.
- Since the monopiles are continuing to increase in size, it would be of interest to develop a model of a larger OWT of e.g 12-14MW if data becomes available.

Bibliography

- Amdahl, J., 2010. TMR4205 Buckling and Ultimate Strength of Marine Structures .
- American Petroleum Institute (API), 2011. API RP 2GEO : Geotechnical and Foundation Design Considerations. Recommended practice for geotechnical foundation design consideration .
- Bachynski, E.E., Ormberg, H., 2015. Hydrodynamic modeling of large-diameter bottom-fixed offshore wind turbines, in: ASME 2015 34th International Conference on Ocean, Offshore and Arctic Engineering, American Society of Mechanical Engineers Digital Collection.
- Bak, C., Zahle, F., Bitsche, R., Kim, T., Yde, A., Henriksen, L.C., Natarajan, A., Hansen, M., 2013. Description of the DTU 10 MW reference wind turbine. DTU Wind Energy Report-I-0092 5.
- Dai, L., Ehlers, S., Rausand, M., Utne, I.B., 2013. Risk of collision between service vessels and offshore wind turbines. Reliability Engineering & System Safety 109, 18–31. ISBN: 0951-8320 Publisher: Elsevier.
- DNV GL, 2015. DNVGL-OS-C401 Fabrication and Testing of Offshore Structures .
- DNV GL, 2016. DNVGL-ST-0126: Support structures for wind turbines. DNV GL As, no .
- DNV GL, 2017. DNVGL-RP-C204: Design against accidental loads. See <http://www.dnvgl.com> .
- Equinor, 2019. Equinor's Empire Wind - equinor.com. URL: <https://>

www.equinor.com/no/what-we-do/empirewind.html. library Catalog:
www.equinor.com.

Federal Bureau of Maritime Casualty Investigation, 2019. Investigation_report_118.18 ,
36.

Horn, J.T., 2018. Statistical and modelling uncertainties in the design of offshore wind
turbines Publisher: NTNU.

Liu, Z., Amdahl, J., 2010. A new formulation of the impact mechanics of ship collisions
and its application to a ship–iceberg collision. *Marine Structures* 23, 360–384. ISBN:
0951-8339 Publisher: Elsevier.

Liu, Z., Amdahl, J., 2019. On multi-planar impact mechanics in ship collisions. *Marine
Structures* 63, 364–383. ISBN: 0951-8339 Publisher: Elsevier.

Manwell, J.F., McGowan, J.G., Rogers, A.L., 2010. *Wind energy explained: theory, design
and application*. John Wiley & Sons.

MarineTraffic, . *MarineTraffic: Global Ship Tracking Intelligence | AIS Marine Traf-
fic*. URL: [https://www.marinetraffic.com/en/ais/home/centerx:
-7.2/centery:56.7/zoom:5](https://www.marinetraffic.com/en/ais/home/centerx:-7.2/centery:56.7/zoom:5).

Merkur Offshore, . *Technology – Merkur Offshore*. URL: [https://
www.merkur-offshore.com/technology/](https://www.merkur-offshore.com/technology/). library Catalog: [www.merkur-
offshore.com](http://www.merkur-offshore.com).

Pedersen, P.T., Zhang, S., 1998. On impact mechanics in ship collisions. *Marine Structures*
11, 429–449. ISBN: 0951-8339 Publisher: Elsevier.

Petroleumstilsynet, 2009. Gransking av Big Orange XVIIIs kollisjon med Ekofisk 2/4-W
8.6.2009 , 23.

Phoon, K.K., Kulhawy, F.H., 1999. Characterization of geotechnical variability. *Canadian
geotechnical journal* 36, 612–624. ISBN: 0008-3674 Publisher: NRC Research Press.

Popov, Y.N., Faddeev, O.V., Kheisin, D.E., Yakovlev, A.A., 1969. Strength of ships sailing
in ice. Technical Report. ARMY FOREIGN SCIENCE AND TECHNOLOGY CEN-
TER CHARLOTTESVILLE VA.

Ramberg, H.F., 2011. High energy ship collisions with bottom supported offshore wind
turbines. Ph.D. thesis. Norges teknisk-naturvitenskapelige universitet, Fakultet for . . .

-
- Ramboll Group, . 150 Monopiles in the North Sea push offshore wind into deeper waters. URL: <https://ramboll.com/projects/re/150-monopiles-in-the-north-sea-push-offshore-wind-into-deeper-waters>. library Catalog: ramboll.com.
- Rasekhi Nejad, A., Bachynski, E.E., Moan, T., 2017. On Tower Top Axial Acceleration and Drivetrain Responses in a Spar-Type Floating Wind Turbine, in: ASME 2017 36th International Conference on Ocean, Offshore and Arctic Engineering, American Society of Mechanical Engineers Digital Collection.
- SafetyAtSea.net, . Three crew injured in wind turbine collision – IHS Markit Safety at Sea. URL: <https://safetyatsea.net/news/2020/three-crew-injured-in-wind-turbine-collision/>.
- Siemens Gamesa, 2020. Offshore Wind Turbine SG 14-222 DD I Siemens Gamesa. URL: <https://www.siemensgamesa.com/en-int/products-and-services/offshore/wind-turbine-sg-14-222-dd>. library Catalog: www.siemensgamesa.com.
- Sif Group, 2020. Foundations - Sif Group. URL: <https://sif-group.com/en/wind/foundations>.
- Smilden, E., Sørum, S.H., Bachynski, E.E., Sørensen, A.J., Amdahl, J., 2020. Post-installation adaptation of offshore wind turbine controls. *Wind Energy* 23, 967–985. ISBN: 1095-4244 Publisher: Wiley Online Library.
- Standards Norway, 2004. NORSOK Standard N-004-Design of steel structures, rev. 2. Lysaker: Standards Norway .
- USFOS, 2019. Modelling of large diameter piles in USFOS , 15.
- Velarde, J., 2016. Design of monopile foundations to support the DTU 10MW wind turbine. Master of science, Norwegian University of Science and Technology .
- WindEurope, . Interactive offshore maps. URL: <https://windeurope.org/about-wind/interactive-offshore-maps/>. library Catalog: windeurope.org.
- WindEurope, 2020. Offshore Wind in Europe: Key trends and statistics 2019. Published February .
- Windpower International, 2013. Good foundations: the pros

and cons of monopiles - World Wind Technology. URL:
[http://www.windpower-international.com/features/
featuregood-foundations-the-pros-and-cons-of-monopiles-4158694/](http://www.windpower-international.com/features/featuregood-foundations-the-pros-and-cons-of-monopiles-4158694/).

Yu, Z., Amdahl, J., 2018. A review of structural responses and design of offshore tubular structures subjected to ship impacts. *Ocean Engineering* 154, 177–203. ISBN: 0029-8018 Publisher: Elsevier.

Appendix

Attached to this report is a zip-folder containing a selection of the modeling files used in the analysis in USFOS. These include all details of the models used if it is of desire to examine them further. All analyses mainly uses 3 files, namely the head file, model file and soil file. Files can be found for:

- Largest collision event with parked OWT
- Earthquake event on parked OWT
- Largest collision event with parked OWT, including shell modeling
- Earthquake event on parked OWT, including shell modeling

